Effects of wind loads and floating bridge motion on intercity bus lateral stability

Journal of Wind Engineering & Industrial Aerodynamics 212 (2021) 104589

Contents lists available at ScienceDirect

Journal of Wind Engineering & Industrial Aerodynamics

journal homepage: www.elsevier.com/locate/jweia

Effects of wind loads and floating bridge motion on intercity bus lateral stability

Dragan Sekulic [a,*], Alexey Vdovin [a], Bengt Jacobson [a], Simone Sebben [a], Stian Moe Johannesen [b]

[a] Chalmers University of Technology, Gothenburg, Sweden
[b] The Norwegian Public Road Administration, Oslo, Norway

ARTICLE INFO

Keywords:
Floating bridge
Wind loads
Lateral stability
Vehicle safety
Bus
Vehicle modelling

ABSTRACT

Efficient transportation is an important factor for regional socio-economic growth. Excitations from wind loads and road motions can influence vehicle-driver behaviour in a way that may impair transportation. This is especially true in open areas such as long-span bridges. This paper investigates the influence of wind loads and floating bridge motions on bus lateral stability for the straight concept solution across Bjørnafjorden in Norway. For this investigation, an 8-degree-of-freedom model of a two-axle coach is used. The defined driver model is based on the pure pursuit path tracking method. The vehicle deviation from the path is found to increase with increasing bus speed. This deviation is significant after the vehicle enters the bridge (e.g., over 0.5 m for a speed of 90 km/h). At 108 km/h, the windward rear wheel loses contact, indicating the potential risk of vehicle roll-over. The mean and root-mean-square values of the handwheel steering angle increase with increasing speed, which might cause difficulty for the driver to control the vehicle. Simulation results suggest that the bus can suitably enter the bridge at a lower speed (e.g., 72 km/h) with the possibility of increasing the speed (up to 90 km/h) after approximately 2 km of travelled distance.

1. Introduction

The E39 route in Norway runs along the west coast from the city Kristiansand in the south to the city Trondheim in the north. The route is 1100 km long. Currently, the travel time is approximately 21 h with a low average speed of approximately 50 km/h, mostly due to several ferry connections. The coastal highway route E39 is Norway's largest road project with the main aim of reducing the travel time on this route to 11 h. Reductions in travel time will be achieved by replacing ferries with different types of bridges and tunnels. The Norwegian Public Roads Administration (NPRA) has prepared a *"Development Strategy for the E39 Coastal Highway Route"* to present potential solutions for fjord crossings. Solutions refer to familiar and new technology that has been employed in the offshore sector. The solutions differ depending on the fjord characteristics. With a width of over 5 km and a depth of over 550 m, Bjørnafjorden is challenging to cross, and floating bridges have been considered for this fjord (Fig. 1).

A reduction in travel time will improve the conditions for freight/passenger transportation on the E39 route. On the other hand, due to bad weather conditions (severe wind/waves), floating bridges exhibit motion that can impair vehicle stability and drivers' driving ability and therefore efficient transportation on this route. In addition to bridge motion, wind loads on Bjørnafjorden crossings are also important factors influencing vehicle driving safety (Vegvesen, 2017). During storm conditions, efficient transportation over the Bjørnafjorden floating bridge will depend on appropriate and timely safety measures (e.g., setting up appropriate driving speeds for different vehicle types and different storm conditions, closing the bridge completely or for certain vehicle types). Before establishing good safety measures, it is important to reveal how driver-vehicle systems would behave on the bridge under specific storm conditions. In this way, recommendations/measures for supporting bridge management can be established. In the past, decisions for speed limits on bridges/highways in windy conditions were often based on intuition or subjective experience (Chen and Cai, 2004).

When investigating bridge-vehicle interactions, there are two common approaches. The first approach considers the mechanism where the bridge and vehicle make one coupled system. The second approach refers to the mechanism where bridge motion is used only as an input for vehicle motion and where the effect of vehicle motion on the bridge is considered insignificant (Siringoringo and Fujino, 2012). For this paper,

* Corresponding author.
E-mail addresses: dragan.sekulic@chalmers.se (D. Sekulic), alexey.vdovin@chalmers.se (A. Vdovin), bengt.jacobson@chalmers.se (B. Jacobson), simone.sebben@chalmers.se (S. Sebben), stian.moe.johannesen@vegvesen.no (S.M. Johannesen).

https://doi.org/10.1016/j.jweia.2021.104589
Received 26 October 2020; Received in revised form 26 February 2021; Accepted 28 February 2021
Available online xxxx

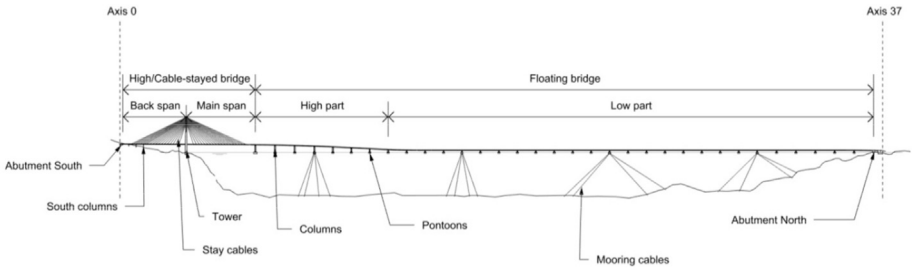

Fig. 1. Straight concept solution for the Bjørnafjorden floating bridge.

in the process of establishing a *bridge-vehicle-wind system,* a second approach is used since the mass of the floating bridge is much higher than the mass of the considered vehicle. Furthermore, one single vehicle is considered in the investigation, absent the presence of vehicle flow on the floating bridge.

The first aim of this paper is to establish a *bridge-vehicle-wind system* and investigate the influence of floating bridge motion and wind loads on vehicle-driver behaviour. The second aim is to investigate vehicle stability for one vehicle type and specific storm conditions (the 1-year storm condition case). The final goal of this investigation is to recommend an appropriate speed for safe vehicle driving across the Bjørnafjorden floating bridge (north-south direction). For this investigation, a model of two-rigid-axle intercity buses of 8-degree-of-freedom (DOF) and a driver model were defined. MATLAB/Simulink software was used for numerical simulation.

2. Vehicle model

For vehicle stability investigation, a two-rigid-axle intercity bus model with 8 degrees of freedom (DOFs) was defined. The in-road-plane DOFs are the total vehicle (m) lateral motion and yaw motion (y, ψ) (Fig. 2a), while the out-of-road-plane DOFs include the sprung mass (m_s) bouncing, front axle (m_{u1}) bouncing, rear axle (m_{u2}) bouncing, roll motions of the sprung mass, and front and rear axles (z, z_1, z_2, ϕ_{xs}, ϕ_{x1}, and ϕ_{x2}) (Fig. 2b). The notations in Fig. 2 and the vehicle parameters and their values are shown in Tables 1 and 2 in the Appendix. These values were obtained from the literature (Jacobson et al., 2020; William et al., 2014; Sekulic et al., 2013; Drugge and Juhlin, 2010; Juhlin, 2009) and are considered to be representative within this category of vehicles.

It was considered that the suspension system at the front axle contains two air springs, four shock absorbers and an anti-roll bar. The suspension system at the rear axle includes four air springs, four shock absorbers and an anti-roll bar. The bus has two steering wheels on the front axle and two dual wheels on the rear axle. These suspension system elements and wheel configurations are standard for intercity buses (Sekulic et al., 2013; Juhlin, 2009; Yu, 2007).

In addition, the following assumptions have been considered:

- The bus runs at a constant forward speed (traction and braking compensate for driving resistance);
- The pitch motion of the bus body is not considered since the vertical bridge displacement has very long wavelengths;
- The bus is symmetrical relative to the longitudinal centre of gravity axis (x-axis);
- All springs and damper elements have linear characteristics;
- The bus body and axles are rigid bodies;
- Axles can roll and bounce with respect to the bus body to which they are attached;
- The centre of gravity (CoG) of the sprung mass coincides with the CoG of the total vehicle since the mass of the bus body is considerably higher than the masses of the bus axles;
- Roll centres (RCs) for the axles coincide with their CoGs;

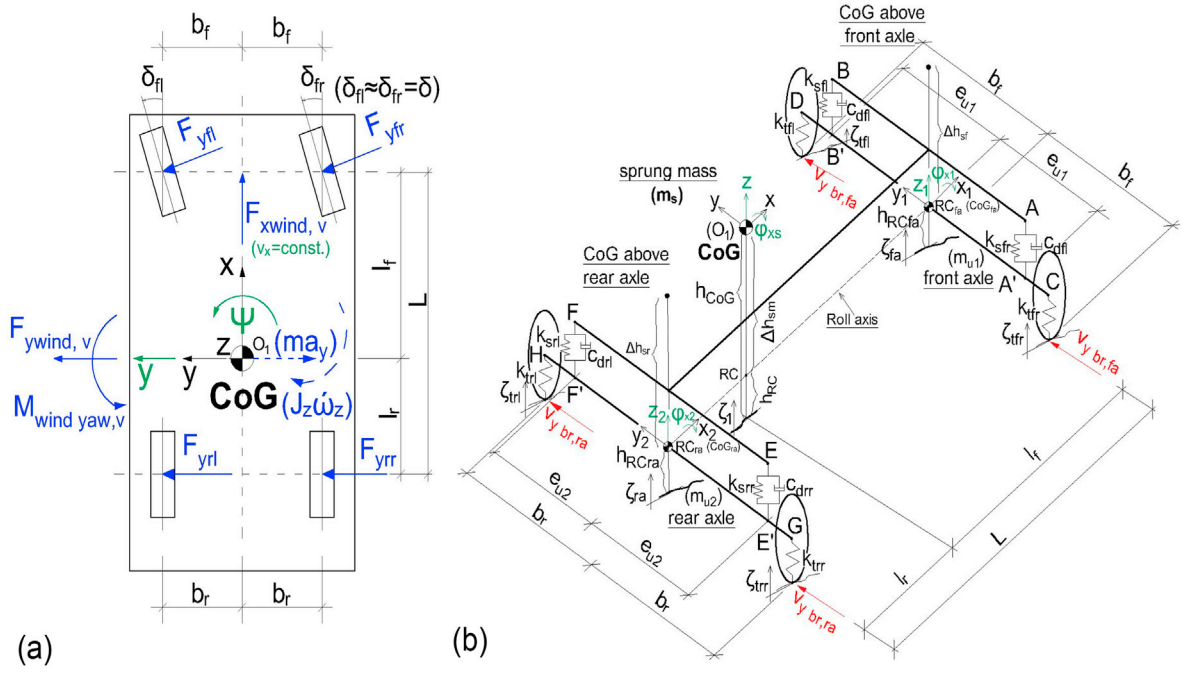

Fig. 2. Vehicle a) in-plane motions, view from above; b) out-of-plane motions.

2.1. In-road-plane

In-plane motions for the whole vehicle (Fig. 2a) are described by Eqs. (1) and (2). When forming differential equations of motion (EOMs), relative to the Earth, the velocity vector of the vehicle CoG is decomposed into its components (v_x and v_y) in the fixed vehicle coordinate system that rotates with an angular velocity (ω_z). The conventional form of EOMs for lateral dynamics remains in this case. Vehicle lateral equilibrium is defined by Eq. (1), and vehicle yaw equilibrium around the z-axis (Fig. 2a) by Eq. (2)

$$m\left(\dot{v}_y + v_x\omega_z\right) = F_{yfl}cos\delta + F_{yfr}cos\delta + F_{yrl} + F_{yrr} + F_{ywind,v} \tag{1}$$

$$J_z\dot{\omega_z} = \left(F_{yfl} - F_{yfr}\right)sin\delta b_f + \left(F_{yfl} + F_{yfr}\right)cos\delta l_f - \left(F_{yrl} + F_{yrr}\right)l_r + M_{wind\ yaw,v} \tag{2}$$

where F_{yfl}, F_{yfr}, F_{yrl}, and F_{yrr} are tyre lateral forces; $F_{ywind,v}$ is the wind force in the lateral direction; and $M_{wind\ yaw,v}$ is the component of the wind moment about the vehicle z-axis. The longitudinal equilibrium is not included since constant longitudinal speed is assumed.

2.2. Out-of-road-plane

Free-body diagrams of sprung and unsprung masses, including active and fictive forces in the vertical direction, are presented in Fig. 3.

Here, the forces F_{sfl}, F_{sfr}, F_{srl}, and F_{srr} are associated with the suspension springs and dampers on the left/right side of the front/rear bus axle, respectively. The forces depend on the relative motion between the sprung and unsprung masses, and their magnitudes can be calculated by Eqs. (3)–(6).

$$F_{sfr} = k_{sfr}(z_A - z_{A'}) + c_{dfr}(\dot{z_A} - \dot{z_{A'}}) = k_{sfr}(z - e_{u1}\phi_{xs} - z_1 + e_{u1}\phi_{x1}) + c_{dfr}(\dot{z} - e_{u1}\dot{\phi_{xs}} - \dot{z_1} + e_{u1}\dot{\phi_{x1}}) \tag{3}$$

$$F_{sfl} = k_{sfl}(z_B - z_{B'}) + c_{dfl}(\dot{z_B} - \dot{z_{B'}}) = k_{sfl}(z + e_{u1}\phi_{xs} - z_1 - e_{u1}\phi_{x1}) + c_{dfl}\left(\dot{z} + e_{u1}\dot{\phi_{xs}} - \dot{z_1} - e_{u1}\dot{\phi_{x1}}\right) \tag{4}$$

$$F_{srr} = k_{srr}(z_E - z_{E'}) + c_{drr}\left(\dot{z_E} - \dot{z_{E'}}\right) = k_{srr}(z - e_{u2}\phi_{xs} - z_2 + e_{u2}\phi_{x2}) + c_{drr}(\dot{z} - e_{u2}\dot{\phi_{xs}} - \dot{z_2} + e_{u2}\dot{\phi_{x2}}) \tag{5}$$

$$F_{srl} = k_{srl}(z_F - z_{F'}) + c_{drl}(\dot{z_E} - \dot{z_{E'}}) = k_{srl}(z + e_{u2}\phi_{xs} - z_2 - e_{u2}\phi_{x2}) + c_{drl}\left(\dot{z} + e_{u2}\dot{\phi_{xs}} - \dot{z_2} - e_{u2}\dot{\phi_{x2}}\right) \tag{6}$$

Out-of-plane motions in the vertical direction for sprung and unsprung masses are presented in Eqs. (7)–(16). Coordinate systems attached to the CoGs of the rigid bodies were in their static equilibrium positions, and weight terms do not appear in the EOMs. Newton's second law was applied when defining the EOMs.

The vertical motion of the sprung mass is described by Eqs. (7) and (8).

$$m_s\ddot{z} = -F_{sfl} - F_{sfr} - F_{srl} - F_{srr} + F_{zwind,v} \tag{7}$$

where F_{sfl}, F_{sfr}, F_{srl}, and F_{srr} are forces from the bus suspension system and $F_{zwind,v}$ is the wind force component in the vertical direction.

$$m_s\ddot{z} = -\left(c_{df_{eq}} + c_{dr_{eq}}\right)\dot{z} - \left(k_{sf_{eq}} + k_{sr_{eq}}\right)z + c_{df_{eq}}\dot{z}_1 + k_{sf_{eq}}z_1 + c_{dr_{eq}}\dot{z}_2 + k_{sr_{eq}}z_2 + F_{zwind,v} \tag{8}$$

The vertical motion of the front axle is described by Eqs. (9)–(12).

$$m_{u1}\ddot{z}_1 = F_{sfl} + F_{sfr} - F_{tfl,dyn} - F_{tfr,dyn} \tag{9}$$

where $F_{tfl,dyn}$ and $F_{tfr,dyn}$ are the tyre dynamic forces due to tyre deflection in the vertical direction. The magnitudes of these forces are calculated by Eqs. (10) and (11).

$$F_{tfl,dyn} = k_{tfl}\left(z_D - \zeta_{tfl}\right) = k_{tfl}\left(z_1 + b_f\phi_{x1} - \zeta_{tfl}\right) \tag{10}$$

$$F_{tfr,dyn} = k_{tfr}\left(z_C - \zeta_{tfr}\right) = k_{tfr}\left(z_1 - b_f\phi_{x1} - \zeta_{tfr}\right) \tag{11}$$

$$m_{u1}\ddot{z}_1 = -c_{df_{eq}}\dot{z}_1 - \left(k_{sf_{eq}} + k_{tf_{eq}}\right)z_1 + c_{df_{eq}}\dot{z} + k_{sf_{eq}}z + k_{tfr}\zeta_{tfr} + k_{tfl}\zeta_{tfl} \tag{12}$$

Similarly, the vertical motion of the rear axle is described by Eqs. (13)–(16).

$$m_{u2}\ddot{z}_2 = F_{srl} + F_{srr} - F_{trl,dyn} - F_{trr,dyn} \tag{13}$$

where $F_{trl,dyn}$ and $F_{trr,dyn}$ are the tyre dynamic forces due to tyre deflection in the vertical direction. The magnitudes of these forces are calculated by Eqs. (14) and (15).

$$F_{trl,dyn} = k_{trl}\left(z_H - \zeta_{trl}\right) = k_{trl}\left(z_2 + b_r\phi_{x2} - \zeta_{trl}\right) \tag{14}$$

$$F_{trr,dyn} = k_{trr}\left(z_G - \zeta_{trr}\right) = k_{trr}\left(z_2 - b_r\phi_{x2} - \zeta_{trr}\right) \tag{15}$$

$$m_{u2}\ddot{z}_2 = -c_{dr_{eq}}\dot{z}_2 - \left(k_{sr_{eq}} + k_{tr_{eq}}\right)z_2 + c_{dr_{eq}}\dot{z} + k_{sr_{eq}}z + k_{trr}\zeta_{trr} + k_{trl}\zeta_{trl} \tag{16}$$

Free-body diagrams of the sprung and unsprung masses (rear axle),

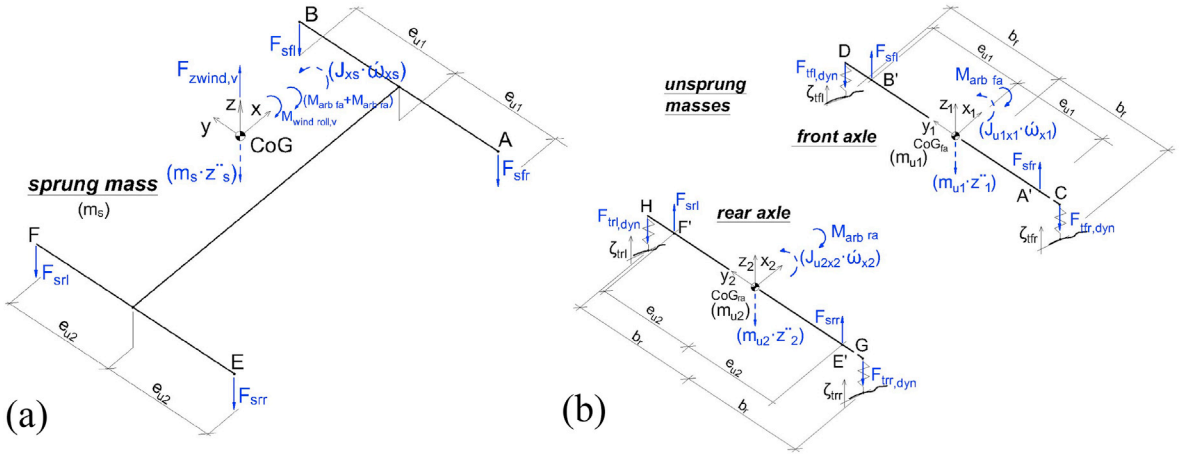

Fig. 3. Free-body diagrams for vertical dynamics a) sprung mass; b) unsprung masses (front/rear axle).

including active forces and moments together with fictive moments for roll dynamics, are presented in Fig. 4. The free-body diagram for the front axle is not presented here but is similar to that for the rear axle but with different notations (Table 1).

The out-of-plane roll motion for the bus sprung/unsprung masses is described by Eqs. (17)–(24). The roll equilibrium equations are written about the point RC (point on the vehicle roll-axis, Fig. 2b) applying D'Alembert's principle. Subsequently, EOMs are defined. The roll equilibrium of the bus body is described by Eqs. (17)–(20),

$$J_{sx}\dot{\omega_{xs}} = (m_s g - F_{z\ wind,v})\Delta h_{sm}\phi_{xs} + m_s a_y \Delta h_{sm} + (F_{sfr} - F_{sfl})e_{u1} + (F_{srr} - F_{srl})e_{u2} - M_{arb,fa} - M_{arb,ra} + M_{wind\ roll,v} \quad (17)$$

where $M_{arb,fa}$ and $M_{arb,ra}$ are respectively moments due to the anti-roll bar on the bus front/rear axle and $M_{wind\ roll,v}$ is the influence from aerodynamic loads (see section 2.4).

$$J_{sx}\dot{\omega_{xs}} = (m_s g - F_{z\ wind,v})\Delta h_{sm}\phi_{xs} + m_s a_y \Delta h_{sm} - K_{\phi f}(\phi_{xs} - \phi_{x1}) - K_{\phi r}(\phi_{xs} - \phi_{x2}) - C_{\phi f}(\omega_{xs} - \omega_{x1}) - C_{\phi r}(\omega_{xs} - \omega_{x2}) - K_{arb_f}(\phi_{xs} - \phi_{x1}) - K_{arb_r}(\phi_{xs} - \phi_{x2}) + M_{wind\ roll,v} \quad (18)$$

where K_{arbf} and K_{arbr} are respectively the anti-roll bar stiffness on the front/rear axle and $K_{\phi f}$, $K_{\phi r}$, $C_{\phi f}$, and $C_{\phi r}$ are respectively the roll stiffness and roll damping for the front/rear axle and are calculated by Eqs. (19) and (20),

$$K_{\phi f} = \frac{1}{2}k_{sfl}(2e_{u1})^2;\ K_{\phi r} = \frac{1}{2}k_{srl}(2e_{u2})^2 \quad (19)$$

$$C_{\phi f} = \frac{1}{2}c_{dfl}(2e_{u1})^2;\ C_{\phi r} = \frac{1}{2}c_{drl}(2e_{u2})^2 \quad (20)$$

The roll motion of the bus front axle is described by Eqs. (21) and (22).

$$J_{u1x1}\dot{\omega}_{x1} = (F_{sfl} - F_{sfr})e_{u1} + (F_{yfl} + F_{yfr})h_{RCfa} + (Z_{tfl} - Z_{tfr})b_f + M_{arb,fa} \quad (21)$$

where Z_{tfl} and Z_{tfr} are the total vertical forces on the front axle left/right wheel, respectively, as described in Eqs. (30)–(33).

$$J_{u1x1}\dot{\omega}_{x1} = K_{\phi f}(\phi_{xs} - \phi_{x1}) + C_{\phi f}(\omega_{xs} - \omega_{x1}) + (F_{yfl} + F_{yfr})cos\delta h_{RCfa} + (z_1 - \phi_{x1}b_f - \zeta_{tfr})k_{tfr}b_f - (z_1 + \phi_{x1}b_f - \zeta_{tfl})k_{tfl}b_f + K_{arb_f}(\phi_{xs} - \phi_{x1}) \quad (22)$$

The roll motion of the bus rear axle is described by Eqs. (23) and (24).

$$J_{u2x2}\dot{\omega}_{x2} = (F_{srl} - F_{srr})e_{u2} + (F_{yrl} + F_{yrr})h_{RCra} + (Z_{trl} - Z_{trr})b_r + M_{arb,ra} \quad (23)$$

where Z_{trl} and Z_{trr} are respectively the total vertical forces on the rear axle left/right wheel, Eqs. (30)–(33).

$$J_{u2x2}\dot{\omega_{x2}} = K_{\phi r}(\phi_{xs} - \phi_{x2}) + C_{\phi r}(\omega_{xs} - \omega_{x2}) + (F_{yrl} + F_{yrr})h_{RCra} + (z_2 - \phi_{x2}b_r - \zeta_{trr})k_{trr}b_r - (z_2 + \phi_{x2}b_r - \zeta_{trl})k_{trl}b_r + K_{arb_r}(\phi_{xs} - \phi_{x2}) \quad (24)$$

Since the bus wheelbase length is small compared to the longitudinal wavelength excitation (see Fig. 17c), the pitch body motion is neglected. Radial damping for heavy vehicle tyres is small (Nguyen and Le, 2019; Liu et al., 2001; Gillespie, 1992) and is therefore also not considered. In the analysis, a bus without passengers is considered, as this configuration would have the lowest mass and hence be maximally sensitive to wind loads.

The vertical distance Δh_{sm} from the CoG to the vehicle roll-axis (point *RC*, Fig. 2b) changes as a function of time and is calculated as

$$\Delta h_{sm} = h_{CoG} - h_{RC} = (h_{CoG,stat.} + (z - \zeta_1)) - h_{RC} \quad (25)$$

where $h_{CoG,\ stat.}$ is the height of the CoG in its static position (Table 1); ζ_1 is the road roughness (Fig. 2b); and h_{RC} is the height of rotational centre (point *RC*) above ground.

The value h_{RC} is determined by Eq. (26):

$$h_{RC} = (l_f h_{RC_{ra}} + l_r h_{RC_{fa}})/L \quad (26)$$

where l_f and l_r are the distances from the front/rear axles to the vehicle CoG (Fig. 2), respectively; h_{RCfa} and h_{RCra} are the heights of the front/rear axle RCs (and heights of the front/rear axle CoGs), respectively.

The values of h_{RCfa} and h_{RCra} can be calculated as follows:

$$h_{RC_{fa}} = h_{RC_{fa},stat.} + (z_1 - \zeta_{fa}) \quad (27)$$

$$h_{RC_{ra}} = h_{RC_{ra},stat.} + (z_2 - \zeta_{ra}) \quad (28)$$

where $h_{RCfa,\ stat}$ and $h_{RCra,\ stat.}$ are respectively the heights of the front/rear axle CoGs in their static positions (Table 1); ζ_{fa} and ζ_{ra} are the corresponding road roughness values below the front/rear axle CoGs (Fig. 2b).

2.3. Tyre forces

The relative lateral velocity of the tyre to the bridge deck has been considered when calculating the lateral tyre slip for the front/rear bus wheels. The lateral tyre forces are calculated using the brush tyre model and depend on a variety of parameters (Eq. (29)). The analytical expression for the brush tyre model can be found in (Jacobson et al., 2020).

$$F_{yfi} = f(C_{cy}, s_{fy}, Z_{fi}, \mu), \quad F_{yri} = f(C_{cy}, s_{ry}, Z_{ri}, \mu),\ (i = l, r) \quad (29)$$

where C_{cy} is the cornering stiffness coefficient (Table 2); Z_{fi} and Z_{ri} are the vertical tyre forces on each wheel; and s_{fy} and s_{ry} are the lateral tyre slip for the wheels on the front/rear axle, respectively.

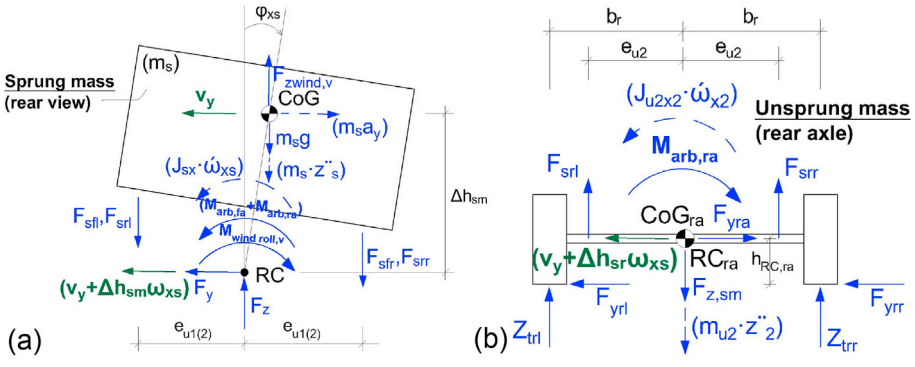

Fig. 4. Free-body diagrams for roll dynamics: a) sprung mass; b) unsprung mass (rear axle).

The vertical forces between the bridge deck and bus front/rear left wheels were defined by Eqs. (30)–(33). The same expressions, but with different notations (see Table 1), apply for the bus front/rear right wheels.

$$Z_{tfl} = Z_{tfl,st} - \frac{\Delta Z_{Mwind\ pitch,v}}{2} + Z_{tfl,dyn} \tag{30}$$

$$Z_{trl} = Z_{trl,st} + \frac{\Delta Z_{Mwind\ pitch,v}}{2} + Z_{trl,dyn} \tag{31}$$

$$Z_{tfl,st} = \frac{mgl_r}{2L};\ Z_{trl,st} = \frac{mgl_f}{2L} \tag{32}$$

$$\Delta Z_{Mwind\ pitch,v} = \frac{M_{wind\ pitch,v}}{L} = \frac{1}{2}\rho V_{rel}^2 A c_P(\beta_w) \tag{33}$$

where $Z_{tfl,st}$ and $Z_{trl,st}$ are respectively the static parts of the vertical forces on the front/rear left wheel and $\Delta Z_{Mwind\ pitch,v}$ is the vertical load transferred from the front to the rear axle due to the wind pitching moment. Eqs. (30)–(33) are derived from pitch equilibrium of the whole vehicle.

Assuming small longitudinal tyre slip, a combined tyre slip model was not previously considered. The lateral tyre slip for the wheels on the front/rear axle is given by Eqs. (34) and (35)

$$s_{fy} = \frac{\Delta v_{fi}}{v_x} - \delta = \frac{\left(v_y + \Delta h_{sf}\cdot\omega_{xs} + l_f\omega_z\right) - v_{y\ br,fa}}{v_x} - \delta,\ (i = l, r) \tag{34}$$

$$s_{ry} = \frac{\Delta v_{ri}}{v_x} = \frac{\left(v_y + \Delta h_{sr}\cdot\omega_{xs} - l_r\omega_z\right) - v_{y\ br,ra}}{v_x},\ (i = l, r) \tag{35}$$

where Δv_{fi} and Δv_{ri} are respectively the relative lateral velocities between the front/rear tyres and bridge deck at the contact point; v_y is the lateral velocity of the whole vehicle; Δh_{sf} and Δh_{sr} are respectively the vertical distances from the CoG of the bus sprung mass to the front/rear axle RCs (Fig. 2b); ω_{xs} is the sprung mass roll rate; $v_{y\ br,fa}$ and $v_{y\ br,ra}$ are respectively the lateral velocities of the bridge deck at the tyre contact point for the front/rear bus axle; and δ is the steering angle (same for the two front wheels).

The vertical distances Δh_{sf} and Δh_{sr} are not static values but depend on the vertical motion of the sprung and unsprung masses, as described in Eqs. (36) and (37):

$$\Delta h_{sf} = \left(h_{CoG_{sm},stat.} - h_{RC_{fa},stat.}\right) + \left(z_s - z_1\right) \tag{36}$$

$$\Delta h_{sr} = \left(h_{CoG_{sm},stat.} - h_{RC_{ra},stat.}\right) + \left(z_s - z_2\right) \tag{37}$$

where $h_{CoGsm,\ stat.}$ is the height of the sprung mass CoG in its static position and where $h_{RCfa,\ stat}$ and $h_{RCra,\ stat.}$ are respectively the heights of the front/rear axle RCs (CoGs) in their static positions (Table 1 in the appendix).

As an example, Fig. 5 shows the lateral bridge velocities for the tyre slip calculation as a function of time at a speed of 90 km/h. The input velocity signals differ slightly due to the bus wheelbase distance (Fig. 5b). The lateral bridge velocity values lie within ±0.2 m/s.

2.4. Aerodynamic loads

The aerodynamic coefficients were determined using Computational Fluid Dynamics (CFD) simulations and verified experimentally using a model-scale wind tunnel (Hellsten et al., 2020). In the wind tunnel, the vehicle was mounted on a rotating turning table allowing full spectrum of wind yaw angles. In CFD, the moving road and wheel rotation were considered following a common method for external aerodynamic simulations (Schuetz, 2015). To simplify the wind tunnel tests and the numerical simulations, the bridge deck section was not considered when determining the aerodynamic coefficients of the vehicle. This facilitated

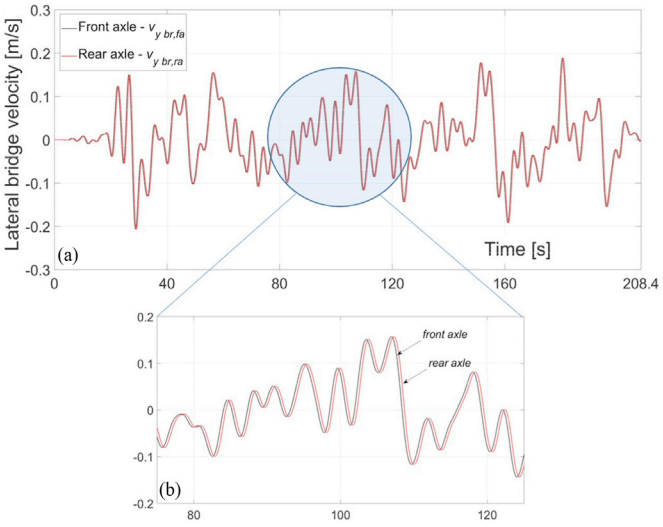

Fig. 5. Vehicle model tyre input a) lateral bridge velocity for the wheels on the front/rear bus axle; b) magnified view for a speed of 90 km/h.

the validation of the CFD method and reduced the computational time. The assumption is a common practice in this type of studies, for example in (Salati et al., 2018; Zhang et al., 2020).

Fig. 6 shows aerodynamic forces and moments coefficients as a function of wind yaw angle, β_w, obtained from CFD simulations.

Fig. 7 shows a bus model used in CFD simulations with a coordinate system (ISO 4130) attached to reference point O. The reference point was set up in the ground plane at the mid-wheelbase and mid-track positions. A sign convention for aerodynamic coefficients is also given in Fig. 7 (arrows indicate positive directions). The coordinate system (ISO 8855) attached to vehicle CoG is also presented in Fig. 7. The positions of the vehicle CoG and RC are given in the same figure.

Aerodynamic forces acting on the vehicle and moments around the vehicle *x*-, *y*- and *z*-axes were calculated by Eqs. (38)-(43):

$$F_{xwind,v} = sign(Vrel\ wind, x)\cdot\frac{1}{2}\rho V_{rel}^2\cdot A\cdot c_d(\beta_w) \tag{38}$$

$$F_{ywind,v} = sign(Vrel\ wind, y)\cdot\frac{1}{2}\rho V_{rel}^2\cdot A\cdot c_S(\beta_w) \tag{39}$$

$$F_{zwind,v} = \frac{1}{2}\rho V_{rel}^2\cdot A\cdot c_l(\beta_w) \tag{40}$$

$$M_{wind\ roll,v} = (-1)\cdot\frac{1}{2}\rho V_{rel}^2\cdot A\cdot L\cdot\left(c_R(\beta_w) + \frac{h_{CoG} - h_{RC}}{L}\cdot c_S(\beta_w)\right) \tag{41}$$

$$M_{wind\ pitch,v} = (-1)\cdot\frac{1}{2}\rho V_{rel}^2\cdot A\cdot L\cdot\left(c_P(\beta_w) + \frac{l_f - L/2}{L}\cdot c_l(\beta_w) - \frac{h_{CoG}}{L}\cdot c_d(\beta_w)\right) \tag{42}$$

$$M_{wind\ yaw,v} = \frac{1}{2}\rho V_{rel}^2\cdot A\cdot L\cdot\left(c_Y(\beta_w) - \frac{l_f - L/2}{L}\cdot c_S(\beta_w)\right) \tag{43}$$

where $F_{xwind,v}$, $F_{ywind,v}$ and $F_{zwind,v}$ are wind forces acting on the vehicle CoG along the *x*-, *y*- and *z*-axes, respectively; $M_{wind\ roll,v}$, $M_{wind\ pitch,v}$ and $M_{wind\ yaw,v}$ are the wind moment components about the vehicle *x*-, *y*- and *z*-axes, respectively; V_{rel} is the relative wind velocity; A is a bus frontal area; L is the bus wheelbase; c_d, c_s, c_l, c_P, c_Y, and c_R are aerodynamic coefficients that are functions of the wind yaw (attack) angle β_w; and ρ is the air density;

To calculate the relative wind velocity and wind yaw angle, wind velocity signals from the global (earth) coordinate system (GCS) were

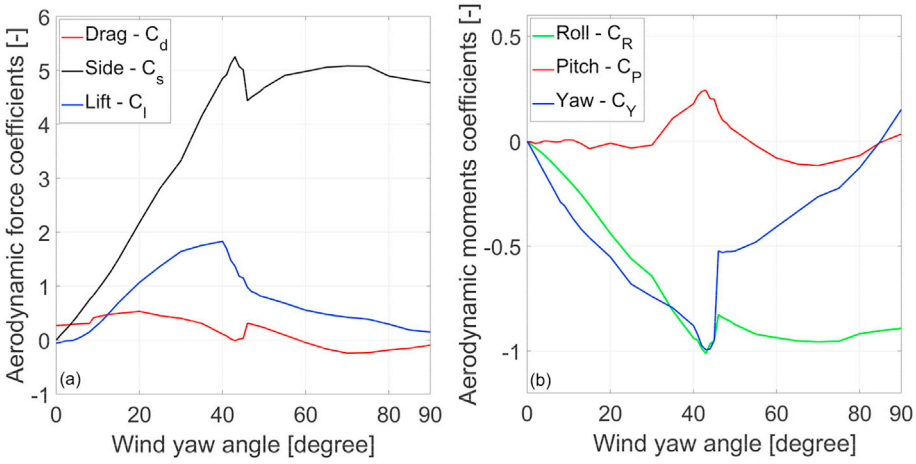

Fig. 6. Aerodynamic coefficients for a) forces; b) moments as a function of the wind yaw angle.

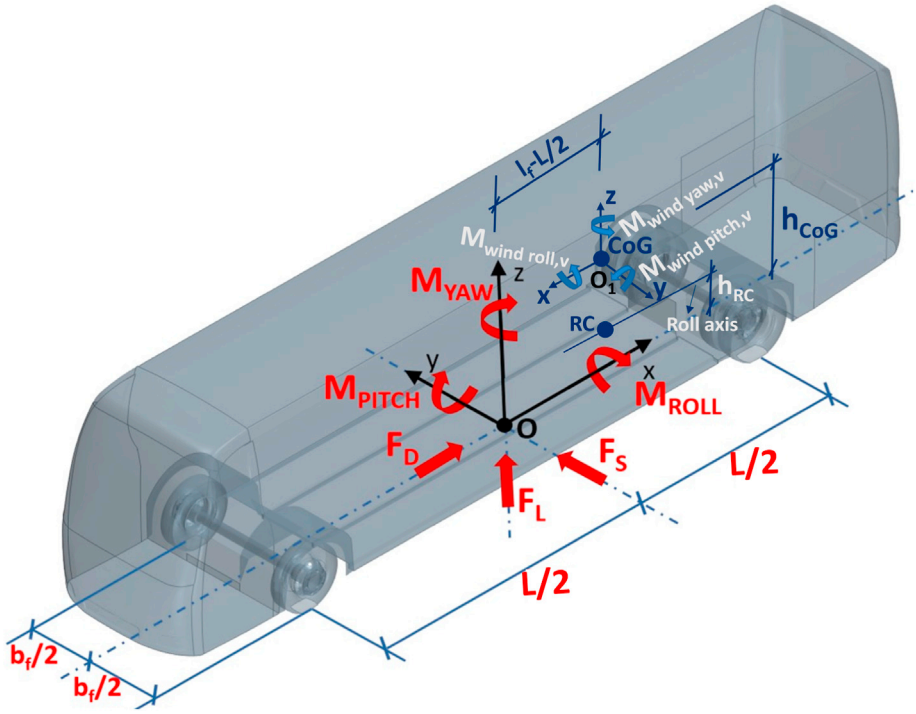

Fig. 7. Bus model with reference points (O, O_1) and coordinate systems (ISO 4130, ISO 8855).

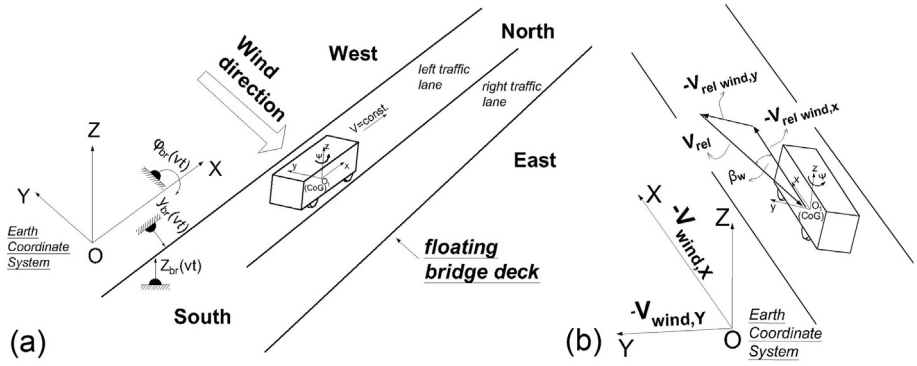

Fig. 8. a) Earth (OXYZ) and vehicle (O_1xyz) coordinate systems; b) wind velocity components.

transformed into the vehicle coordinate system (VCS) O_1xyz (Fig. 8) by Eq. (44). The vertical wind component $V_{wind,Z}$ was considered insignificant compared to the horizontal wind components ($V_{wind,X}$; $V_{wind,Y}$) (see Fig. 18) (Bhat et al., 2020).

$$\{ V_{wind,x} \quad V_{wind,y} \}^T = T_{ve} \{ -V_{wind,X} \quad -V_{wind,Y} \}^T \tag{44}$$

where $V_{wind,x}$ and $V_{wind,y}$ are wind velocities in the VCS; $V_{wind,X}$ and $V_{wind,Y}$ are wind velocities in the horizontal direction in the GCS; and T_{ve} is the linearized transformation matrix from GCS to VCS, Eq. (45).

$$T_{ve} = \begin{bmatrix} \cos(\psi) & \sin(\psi) \\ -\sin(\psi) & \cos(\psi) \end{bmatrix} \approx \begin{bmatrix} 1 & \psi \\ -\psi & 1 \end{bmatrix} \tag{45}$$

where ψ is the vehicle yaw angle.

The relative wind velocity components can be presented as

$$\{ V_{rel\ wind,x} \quad V_{rel\ wind,y} \}^T = \{ V_{wind,x} \quad V_{wind,y} \}^T - \{ v_x \quad v_y \}^T \tag{46}$$

where $V_{rel\ wind,x}$ and $V_{rel\ wind,y}$ are the relative wind velocities along the coordinate axes in the VCS.

The magnitude of the relative wind velocity can be calculated as

$$V_{rel} = \sqrt{V^2_{rel\ wind,x} + V^2_{rel\ wind,y}} \tag{47}$$

The wind yaw angle can be calculated as follows:

$$\beta_w = arctan\left(\frac{V_{rel\ wind,y}}{V_{rel\ wind,x}} \right) \tag{48}$$

Fig. 9a presents the wind yaw angle as a function of distance for five different bus speeds. Generally, lower values of wind yaw angle correspond to higher bus speeds. The calculated side wind forces and wind rolling moments as a function of distance for five bus speeds are presented in Fig. 9b and c. Higher values of the side wind force and rolling moments correspond to higher vehicle speeds, especially when the bus enters the bridge. The high side wind force can influence the lateral displacement from the path that the vehicle is supposed to follow. A high wind rolling moment could cause considerable load transfer from windward to leeward wheels and therefore lead to vehicle roll-over.

3. Driver model

The driver model in this work was defined based on the path tracking pure pursuit method (Snider, 2009). This method geometrically calculates the curvature of a circular arc that connects the rear axle location (point RA) to an aim point on the path in front of the vehicle (point AP) (Fig. 10a). The vehicle motion is assumed to follow *"ideal-tracking"* tyres, i.e., zero sideslip independent of forces.

More specifically, vehicle rear axle position RA (X_{RA}, Y_{RA}) and the position of the aim point AP (X_{AP}, Y_{AP}) on the moving path have been determined (Fig. 10b). When calculating position of the aim point a look-ahead distance s_{la} has been considered from the current rear axle position. Knowing the coordinates of the points RA and AP, angle α can be calculated as:

$$\alpha = \alpha_1 + \psi = \arcsin\left(\frac{Y_{AP} - Y_{RA}}{s_{la}} \right) + \psi \tag{49}$$

where ψ is the vehicle yaw angle.

The steering angle δ can be determined using the aim point location and the angle α, such as

$$\delta = \frac{2L\alpha}{s_{la}} = \frac{2L\alpha}{t_{la} v_x} \tag{50}$$

where α is the angle between the vehicle's heading direction and the look-ahead vector; L is the vehicle wheelbase; t_{la} is the look-ahead time (LAT); and v_x is the constant vehicle longitudinal speed. The handwheel steering angle (HSA) is found through the model by assuming a constant steering ratio.

3.1. Parameter tuning

Tuning the pure pursuit controller was performed by comparing HSA responses from driving simulator tests and numerical simulations. The Hexatech 1CTR driver-in-the-loop motion platform simulator (CASTER) has been extensively used for the investigation of vehicle (passenger car/bus) tracking ability and driver behaviour on Bjørnafjorden floating bridges (Gustafsson et al., 2019; Bhat et al., 2020). Fig. 11 comparatively

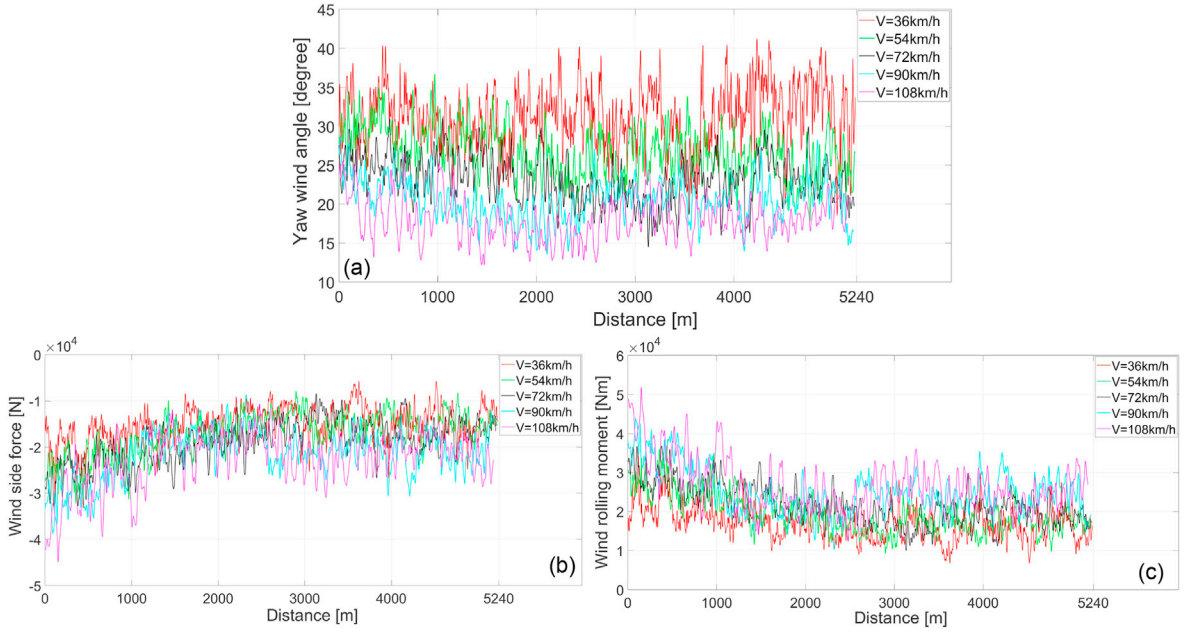

Fig. 9. a) Wind yaw angle; b) wind side force; c) wind rolling moment as a function of distance and vehicle speed.

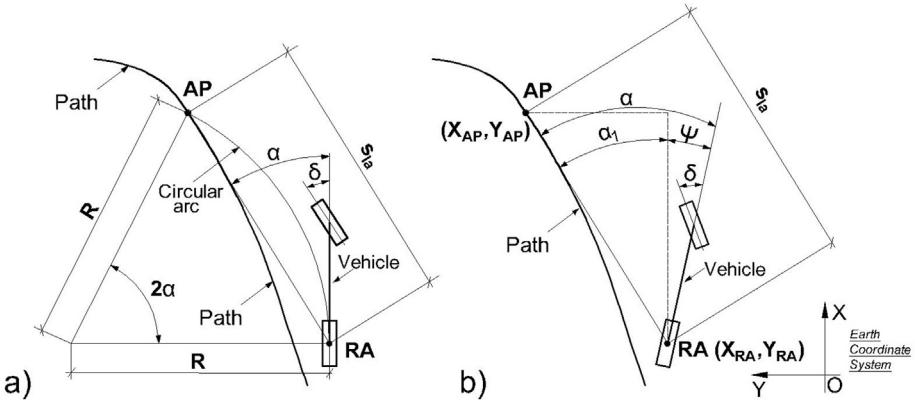

Fig. 10. a) Pure pursuit geometry; b) positions of the characteristic points and characteristic angles.

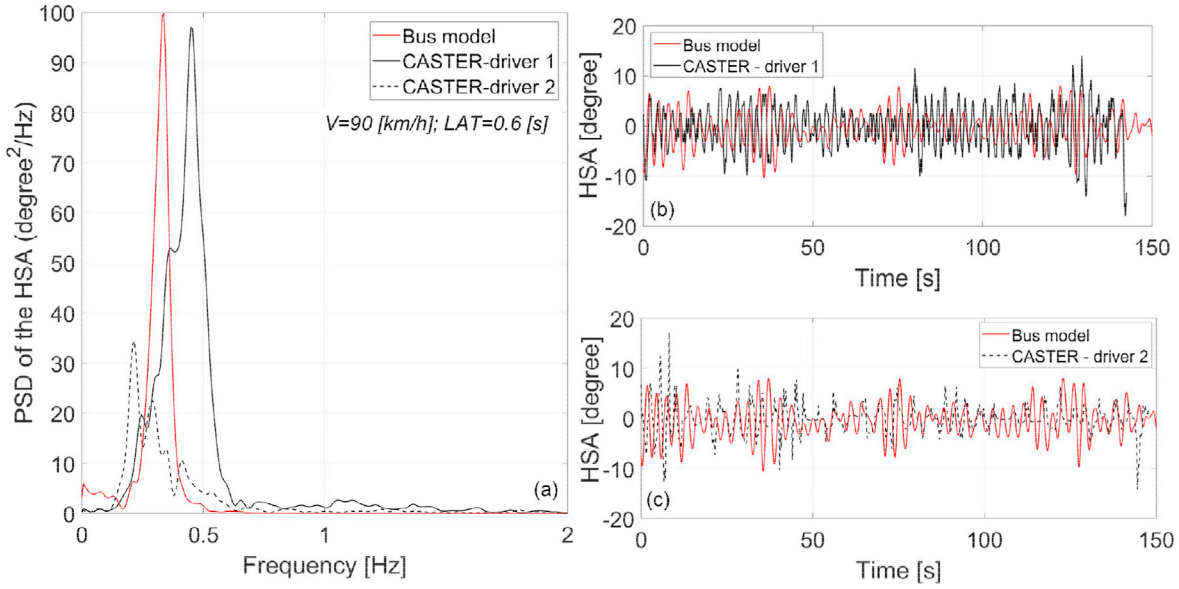

Fig. 11. HSA signals for bus speeds of 90 km/h and LAT = 0.6 s as a function of a) frequency; b) time (driver 1); c) time (driver 2).

shows HSAs from driving simulator tests (two drivers) and from a simulated speed of 90 km/h. In both the test and numerical simulation, the cross-wind velocity component was taken as the wind input. The signal from numerical simulation for the case of 0.6 s of LAT fairly matches both signals from the tests. The magnitudes of the signals are similar (Figure 11(b, c)), but the frequencies are different (Fig. 11a). In the frequency domain, the signal intensities for drivers 1 and 2 differ and are concentrated at approximately 0.5 Hz and 0.25 Hz. However, HSA for 0.6 s of LAT incorporates signal frequencies from both drivers (Fig. 11a). Similarly, an LAT of 0.6 s is confirmed for the 70 km/h vehicle speed case.

Note that the lateral bridge motion path that the vehicle needs to follow is not the same as the path that the driver sees and steers the vehicle to. Fig. 12 shows an example of the path that a vehicle needs to follow and the path that a driver would respond to for a bus speed of 90 km/h. At point 1, the driver model calculates the steering angle considering aim point 2 to reach aim point 3 (Fig. 12b). The paths differ slightly due to the lateral bridge motion.

3.2. Lateral offset

When calculating the vehicle steering angle, the pure pursuit method does not consider the presence of wind components (Snider, 2009). In the path tracking results, lateral offset within the total lateral vehicle displacement appears in numerical simulations. In reality, under the influence of the cross-wind component, the driver steers the vehicle back on the path and then offsets the aim point slightly from the path he or she truly wants to follow. This approach works with slow dynamics since the side wind is essentially constant or at least not shifting direction.

Consequently, the lateral displacement is considered relative to an average straight line. One possible improvement of the driver model based on the pure pursuit method is to add *"steering compensation"*. The appearance of the lateral offset under the influence of the cross-wind load on vehicles with a high side area has also been confirmed in numerical investigations (Zhou and Chen, 2015; Chen and Cai, 2004).

4. Vehicle model excitations

4.1. Bridge motion data and vehicle input data set

Floating bridges were modelled as finite element models in *Orcaflex* software for dynamic analysis and *Sofistik* for static analyses (Vegvesen, 2017). The bridge response time series data were obtained by simulation in *Orcaflex* software, where hydrodynamic loads and wind loads were used as inputs. Simulation of bridge motions under the influence of environmental loads (wind and waves for 1-year storm conditions) was performed for 1 h (3600 s) of simulation time. The structure was excited by waves generated from a Jonswap spectrum with significant wave

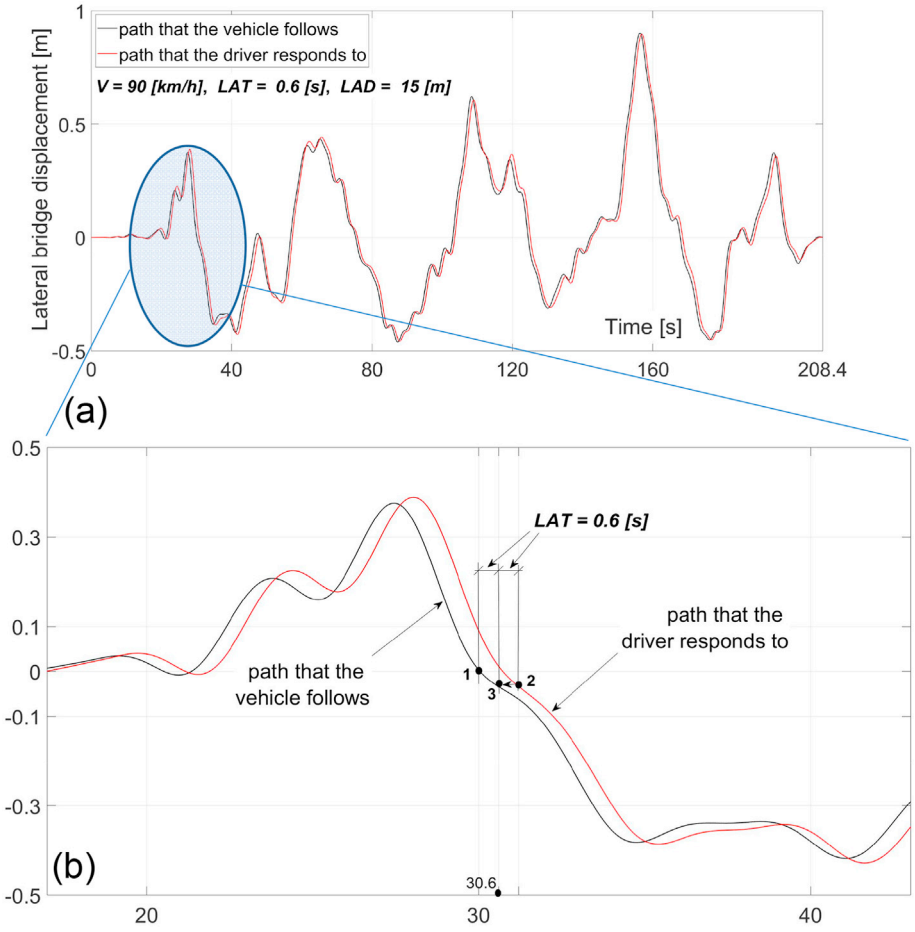

Fig. 12. Path a) that the vehicle needs to follow and that the driver responds to; b) magnified view for a speed of 90 km/h.

height (H_s = 1.2 m) and peak period (T_p = 4.26 s). A wind field was generated from a Kaimal wind spectrum with mean wind speed w_s = 21.40 m/s and along turbulence I_u = 0.15. Small swell waves propagating into the fjord from the North-Sea were also considered (H_s = 0.22 m, T_p = 17 s) (Vegvesen, 2017). Bridge motion data and wind data were collected and stored in *h.5* files.

Vertical (z_{br}), lateral (y_{br}) and torsional (ϕ_{br}) displacements of the bridge deck centre (point C, Fig. 13) were given for specific points along the length of the bridge (on each 5 m or on each 8 m depending on the bridge nodes definition in the *Orcaflex* software).

Vehicle input data set were defined from the bridge motion data. Vehicle input data depend on vehicle position on the bridge deck and on time. Consequently, vehicle inputs will not be the same for different vehicle speed. Fig. 14a presents vertical bridge displacement data for a few points (at 0.6 km; 2 km; 5 km) as a function of simulation time. It could be seen that vertical bridge displacement on distance at 2 km differs for two chosen vehicle speeds of 36 km/h and 90 km/h (Fig. 14b).

Definition of the vehicle input data set is explained in more detail now. Simulation time in our investigation is equal to the vehicle traveling time over the floating bridge and is less than the bridge motion simulation time. For example, simulation time for the vehicle speed at 36 km/h is 524 s whereas simulation time for the bridge motion is 3600 s. Bridge motion data were collected on each 0.2 s in *Orcfalex* software. For the bus speed of 36 km/h, there will be *N* different vehicle inputs, Eq. (51)

$$N = \frac{t_{sim,\,br} - t_{sim,\,v}}{\Delta t} = \frac{3600 - 524}{0.2} = 15380 \tag{51}$$

where $t_{sim,br}$ is the bridge motion simulation time; $t_{sim,v}$ is the vehicle simulation time; Δt is the sampled time for the bridge motion data.

Fig. 15 schematically shows bridge vertical displacement in function of time and distance. In the same figure two examples of the bridge vertical displacements for the vehicle inputs at the speed of 36 km/h have been denoted. Lateral and roll displacements and wind components for the vehicle input data set were obtained in the same way. The size of the vehicle input data differs for different vehicle speeds. Specific inputs for our simulation were defined from the vehicle input data set.

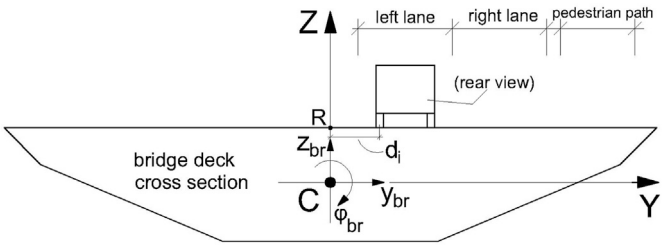

Fig. 13. Bridge deck cross section.

4.1.1. *Vertical excitations of floating bridges*

It has already been confirmed that variation in the vertical tyre forces due to floating bridge motions slightly differ from the case of the stationary road (Sekulic et al., 2020). Wind velocity components, especially the cross-wind component, have significant effects on the heavy vehicle lateral deviation from the path on the floating bridge (Bhat et al., 2020). Vehicle inputs that correspond to the highest *RMS* value of the cross-wind velocity component were extracted from the vehicle input data set. The extracted vertical and roll bridge displacements were used when defining vertical excitations for the left and right wheel tracks of the bus model.

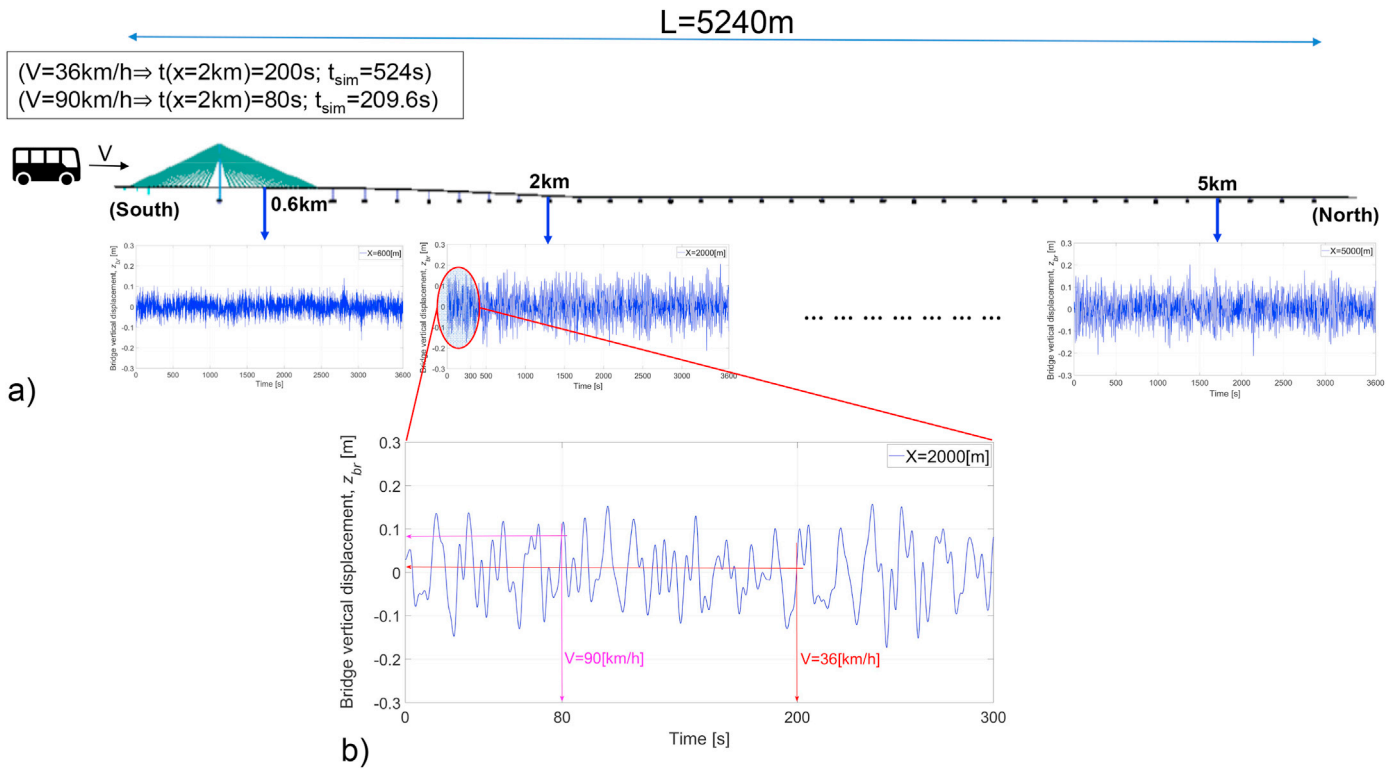

Fig. 14. Vertical bridge displacement a) at distance of 0.6 km, 2 km, 5 km; b) magnified view for distance of 2 km.

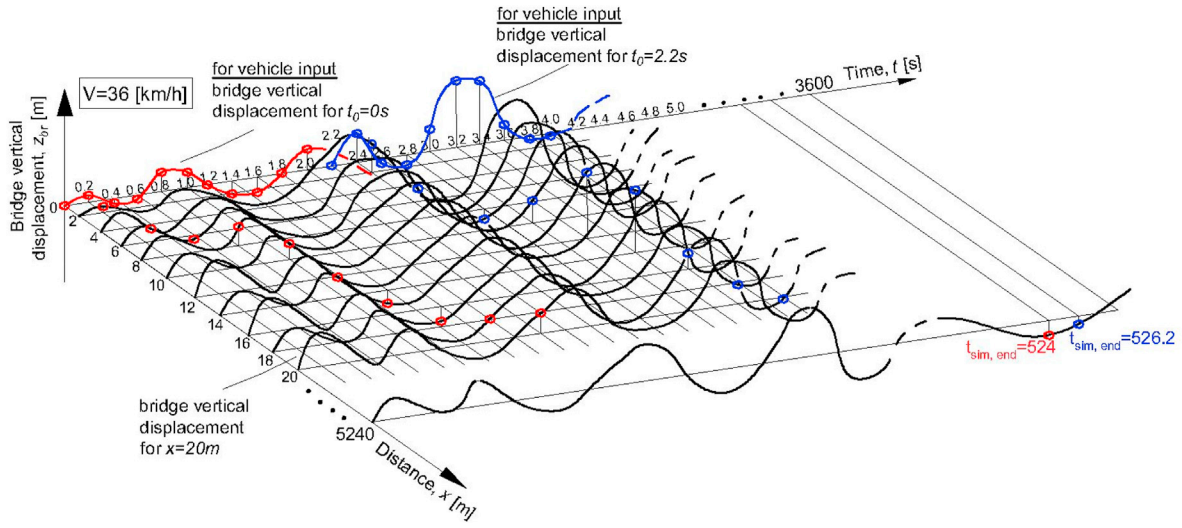

Fig. 15. Bridge vertical displacement as a function of time and distance, and bridge vertical displacements for the vehicle input data set at speed of 36 km/h.

The extracted lateral bridge motion was used as an input for the driver model (e.g. Fig. 12), whereas bridge lateral velocities (e.g. Fig. 5) were used for the tyre lateral slips calculations (Eq. (34), (35)).

A road roughness equivalent to good conditions was considered for the bus model excitations definition. The power spectral density (PSD) of the A/B road class defined in the ISO, 1995 standard was used for road roughness modelling (ISO 8608). A random road profile can be represented by an infinite sum of harmonic functions of different amplitudes, circular frequencies and phase angles, according to Shinozuka (1972). More details about the road modelling process can be found in (Sekulic, 2013, 2018). The length of the modelled road is equal to the length of the Bjørnafjorden floating bridge (5240 m). Fig. 16a shows the road roughness as a function of distance. The roughness magnitudes are distributed mainly within ±0.01 m.

Fig. 16c shows vertical excitation for point R on the bridge deck (see Fig. 13) for five different bus speeds calculated by Eq. (52).

$$\zeta_R(vt) = z_{br}(vt) + \zeta_{rr}(vt) \tag{52}$$

where $\zeta_R(vt)$ is vertical excitations on the bridge deck for point R; $z_{br}(vt)$ is bridge vertical displacement (point C, Fig. 13); $\zeta_{rr}(vt)$ is road roughness modelled by ISO 8608. Fig. 16b comparatively shows vertical bridge displacement ($z_{br}(vt)$) and vertical bridge excitation ($\zeta_R(vt)$) referring to point R for the bridge length of 0.4 km and vehicle speed of 36 km/h. The vertical floating bridge excitations values lie within ±0.2 m (Fig. 16c).

Fig. 16d shows the PSDs of bridge vertical excitations, referring to point R on the bridge deck, presented within the ISO 8608 road classification as a function of angular spatial frequencies. Bridge excitations

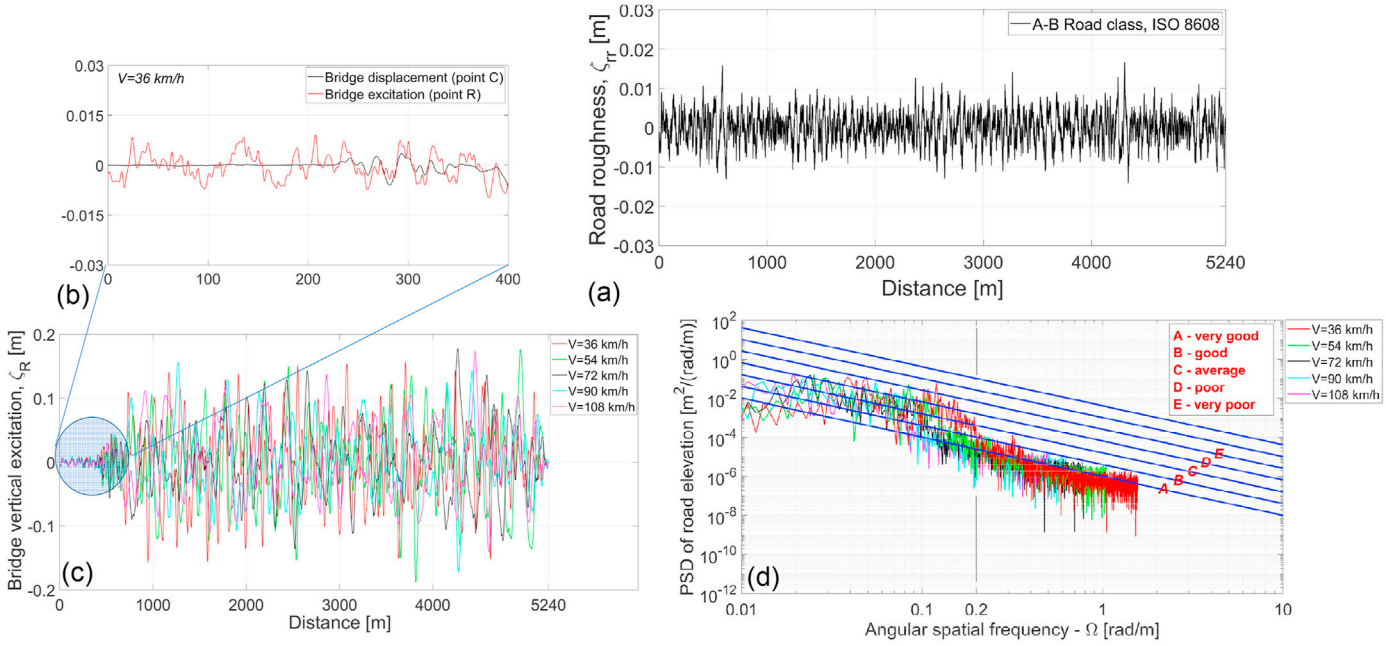

Fig. 16. Vertical excitation a) A/B road class generated from ISO 8608 standard; b) magnified view for vertical bridge displacement and excitation for the speed of 36 km/h; c) vertical bridge excitation as a function of distance and vehicle speed; d) PSDs of vertical floating bridge excitation in the ISO 8608 standard.

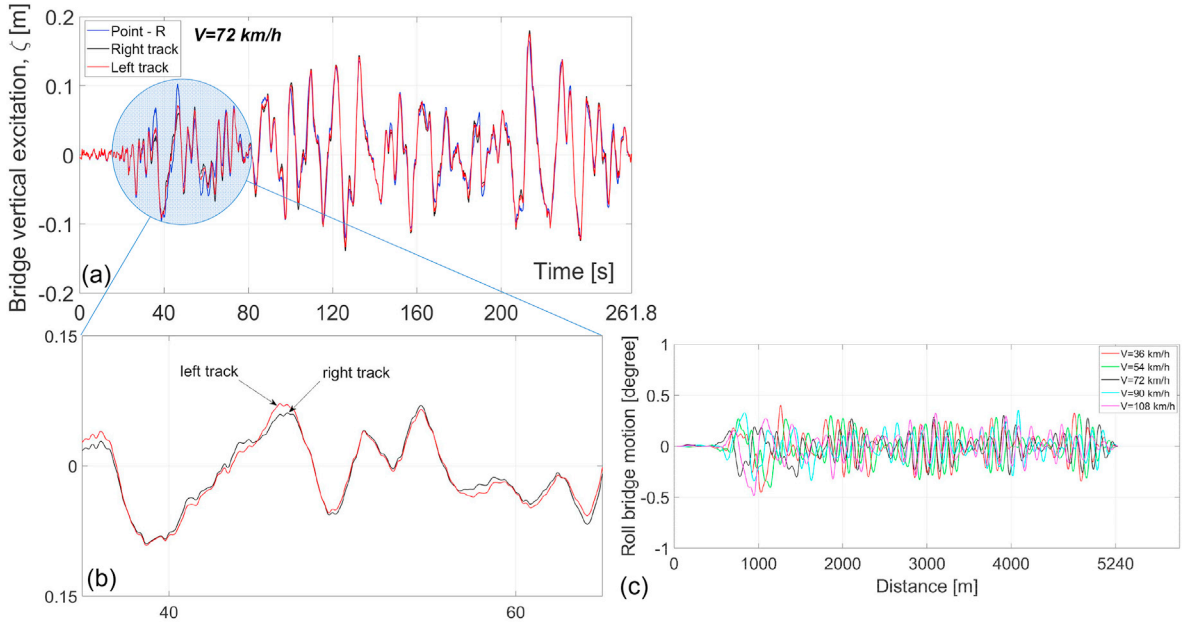

Fig. 17. Vehicle model input a) vertical excitations for point R and on the left/right track for the left lane; b) magnified view for the left/right track for a speed of 72 km/h; c) bridge roll motion as a function of distance and vehicle speed.

with low angular spatial frequencies (long wavelengths) prevail. High PSDs exist at frequencies below 0.2 rad/m. These angular frequencies correspond to road roughnesses with very long wavelengths, according to Eq. (53). Roughnesses on these wavelengths excite vehicles with low frequencies even at high speeds. For example, for the speed of 108 km/h, the frequencies are below 0.1 Hz according to Eq. (54). Roughness at higher angular spatial frequencies (larger than 0.2 rad/m) mainly comes from the A/B road class that was modelled using ISO 8608.

$$\lambda = \frac{2\pi V}{\Omega} \tag{53}$$

$$f = \frac{V}{\lambda} \tag{54}$$

where λ is the wavelength; Ω is the angular spatial frequency; V is the vehicle speed; and f is the frequency.

Vertical excitations on the left and the right bus wheels are obtained by Eq. (55):

$$\zeta_{ti}(vt) = z_{br}(vt) + \zeta_{rr}(vt) + d_i \cdot \phi_{br}(vt), \ \ (i = fl, fr, rl, rr) \tag{55}$$

where d_i is lateral distance from the rotational centre (point C) to the

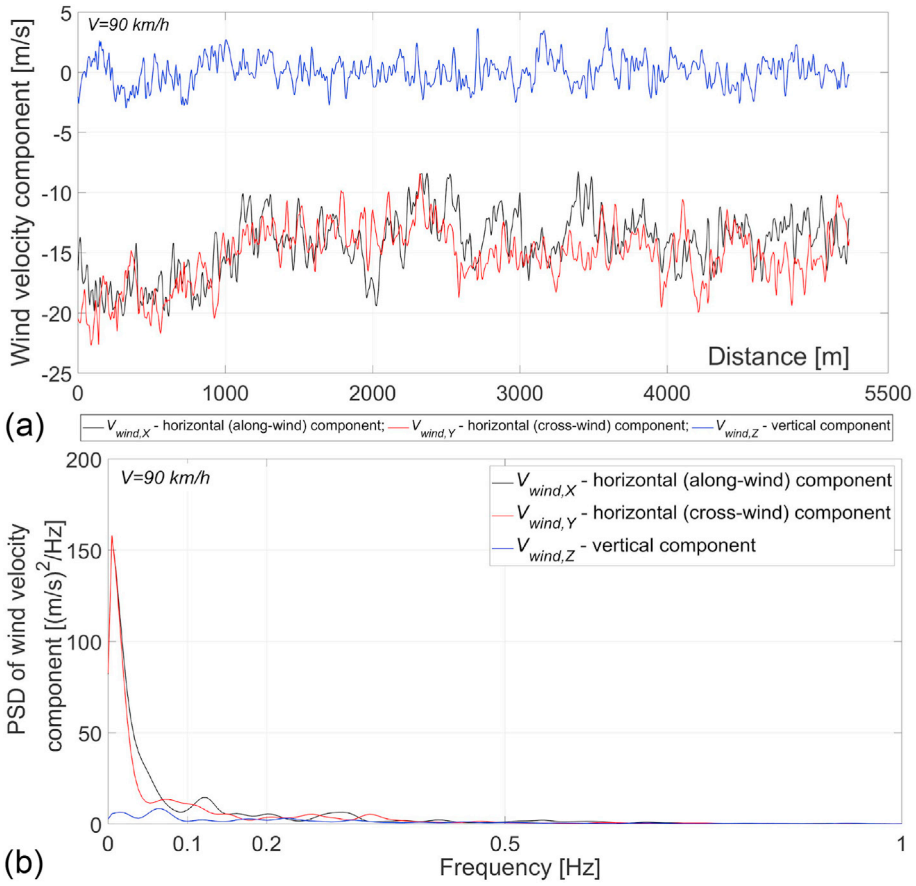

Fig. 18. Wind velocity components in GCS a) as a function of distance; b) as a function of frequency for a speed of 90 km/h.

contact point between the bus wheel and the bridge deck (Fig. 13); $\phi_{br}(vt)$ is roll motion of the bridge deck;

Fig. 17a shows an example for the left/right track vertical excitations for the left traffic lane (Fig. 8a) as a function of time for a bus speed of 72 km/h. Vertical excitations for the left/right bus wheels and for the point R are almost identical meaning that the distribution of the road roughness for these three excitations will not differ in frequency domain. Fig. 17c shows roll-angle bridge motion data as a function of time for five different vehicle speeds. The roll motions for each bus speed are relatively small, within ±0.5°. Vertical bridge excitations for the right traffic lane are considered to be identical to vertical excitations for the left traffic lane due to insignificant bridge roll motion values.

4.1.2. Wind velocity components

A stochastic wind velocity field was generated in *Windsim* software (Vegvesen, 2017). Fig. 18 presents an example of the wind velocity signal defined in the GCS for a vehicle speed of 90 km/h. The along-wind and cross-wind components have larger magnitudes (close to 20 m/s) on the first 1000 m of the travelled distance and decrease to approximately 15 m/s at the end of the bridge (Fig. 18a). The intensity of the mean part of the wind speed logarithmically increases as a function of the height (Branlard, 2010). In the case of Bjørnafjorden crossing, the height of the bridge deck gradually decreases, starting from approximately 70 m in the south to 20 m in the north (Fig. 1). Wind velocity components for other vehicle speeds have similar characteristics and intensities as for 90 km/h (Vegvesen, 2017).

Fig. 18b presents the PSDs of the wind velocity components for a vehicle speed of 90 km/h. Signal intensities are concentrated in the low-frequency range, below 0.2 Hz. The highest intensities for the along-wind and cross-wind components go below 0.1 Hz.

5. Simulation results and discussion

5.1. Risk of lateral lane departure

5.1.1. Path tracking or lateral path deviation

This section presents the results of vehicle lateral displacement (deviation) from the path. As mentioned, lateral offset in the vehicle total lateral displacement is not considered in the discussion. After initial vehicle displacement, the cross-wind driver reacts quickly and steers the vehicle back to the path (Bhat et al., 2020). As found in section 3.2, the driver model gives an almost constant lateral offset, from which the deviation is measured.

As an example, Fig. 19a comparatively shows path tracking with and without wind load considered for a bus speed of 90 km/h. In the case when the wind load is not considered, the vehicle stays on the path, which confirms that the defined driver model correctly works. Under the influence of wind, the bus lateral displacement is maintained around some offset value from the path (Fig. 19b). The lateral offset is equal to the mean value of the lateral displacement and increases with increasing bus speed. This offset has a high value (close to 1 m) for a bus speed of 108 km/h (Fig. 19c).

Pure pursuit tracking method exploits geometric relationships between the vehicle and the path and does not consider cross-wind loads effect on the vehicle lateral offset. However, in reality, under the influence of the cross-wind component, the driver steers the vehicle back on the path eliminating lateral offset. Therefore, offset value is not considered in the analysis of the vehicle lateral path deviation. Having this in mind, authors consider that driver model based on pure pursuit method is suitable for this investigation.

Fig. 20 present vehicle path tracking without lateral offset considered for vehicle speeds of 36 km/h, 90 km/h and 108 km/h. The path

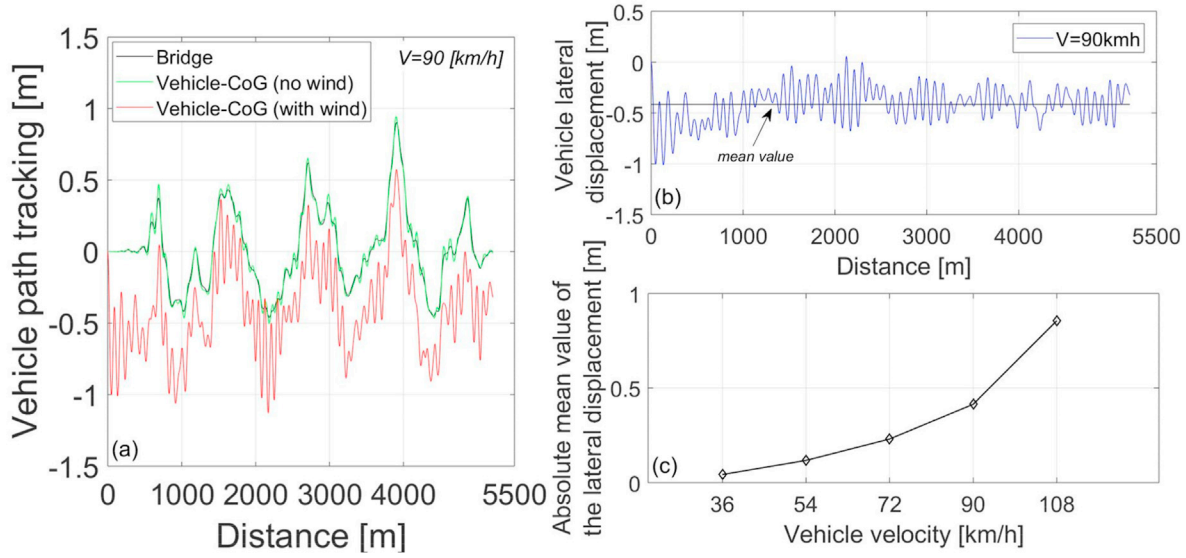

Fig. 19. Simulation results for a) vehicle path tracking; b) lateral displacement from the path; c) absolute mean value of the lateral displacement as a function of vehicle velocity.

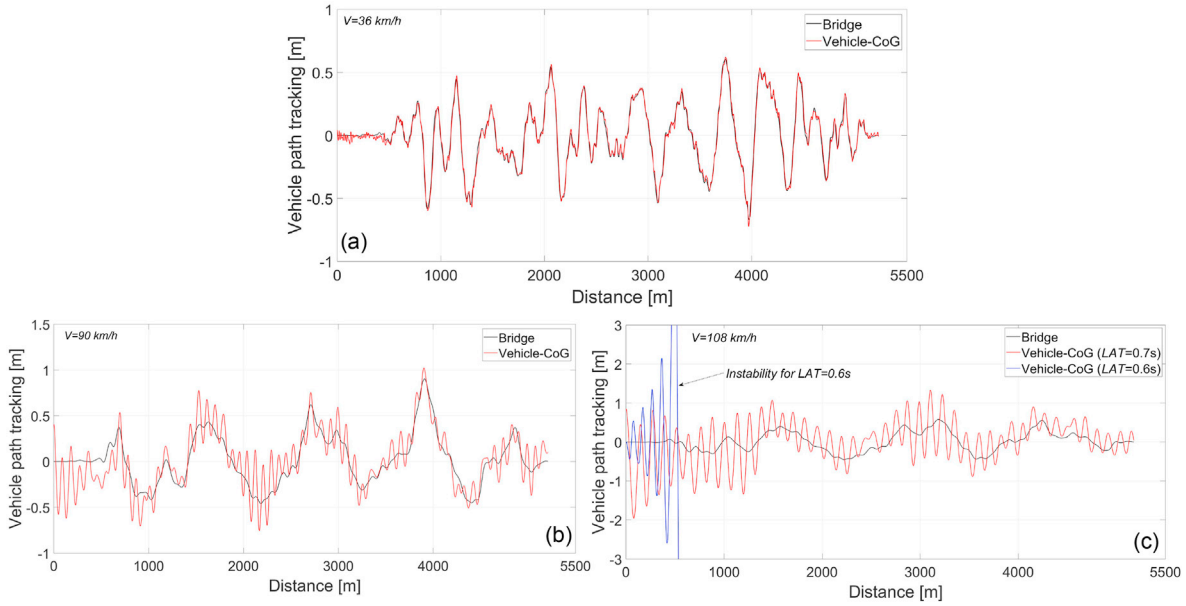

Fig. 20. Path tracking for bus speeds of a) 36 km/h; b) 90 km/h; c) 108 km/h.

deviation increases with increasing bus speed. The deviation is significant after the vehicle enters the bridge, where high-velocity cross-wind loads are present. For a speed of 90 km/h, the deviation is approximately 0.5 m (Fig. 20b), and for a speed of 108 km/h, the vehicle path deviates up to 2 m (Fig. 20c). The simulation results showed that the vehicle is unstable for an LAT of 0.6 s (LAD of 18 m) at a speed of 108 km/h. The vehicle is stable for an LAT of 0.7 s, and this value was taken in the simulation. These results confirm that the vehicle stability for one speed is dependent on the tuning parameter LAT value, which is one of the pure pursuit controller characteristics (Snider, 2009).

Fig. 21 presents simulation results for vehicle deviation from the path for different speeds. The largest path deviations are 108 km/h soon after the bus enters the bridge and remain at a high value (approximately 0.5 m) along the bridge (Fig. 21a). The *RMS* value of the lateral displacement increases with increasing speed (Fig. 21b). The maximal deviation increases with increasing bus speed (Fig. 21c) and is high for a speed of 108 km/h (approximately 2 m). For speeds higher than 83 km/h and 95 km/h, the maximal deviations exceed 0.5 m and 1 m, respectively. The maximal deviations are significant at the beginning of the bridge. Approximately 2 km after entering the bridge, the lateral displacements are close to 0.5 m for the a velocity of 90 km/h (Fig. 21a).

The simulation results suggest that under wind loads from 1-year storm conditions, buses should enter the bridge at lower speeds (e.g., 72 km/h) with the possibility of increasing the speed (up to 90 km/h) after approximately 2 km. This conclusion is similar to recommendations based on driving simulator tests for buses running in straight lines across floating bridges. The recommendation suggests *straight line driving for a bus of* 90 km/h *up to weather 6 (1-year storm condition)* (Bhat et al., 2020).

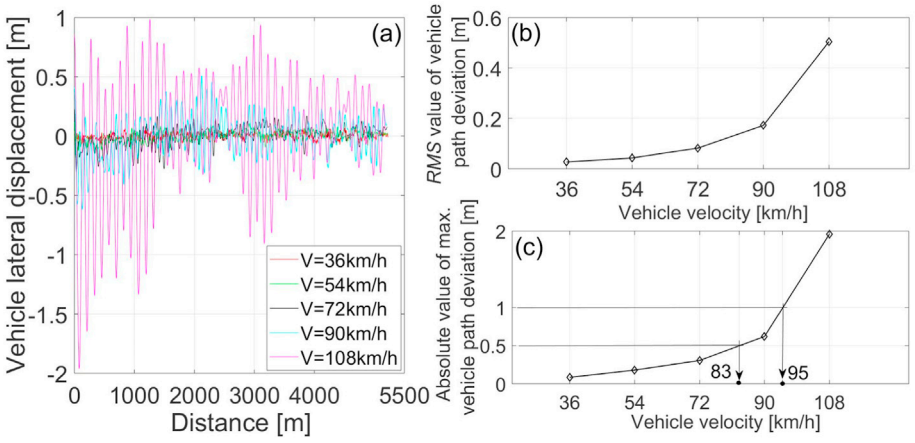

Fig. 21. Simulation results for a) lateral displacement; b) RMS of path deviation as a function of vehicle velocity; c) absolute value of maximal path deviation as a function of vehicle velocity.

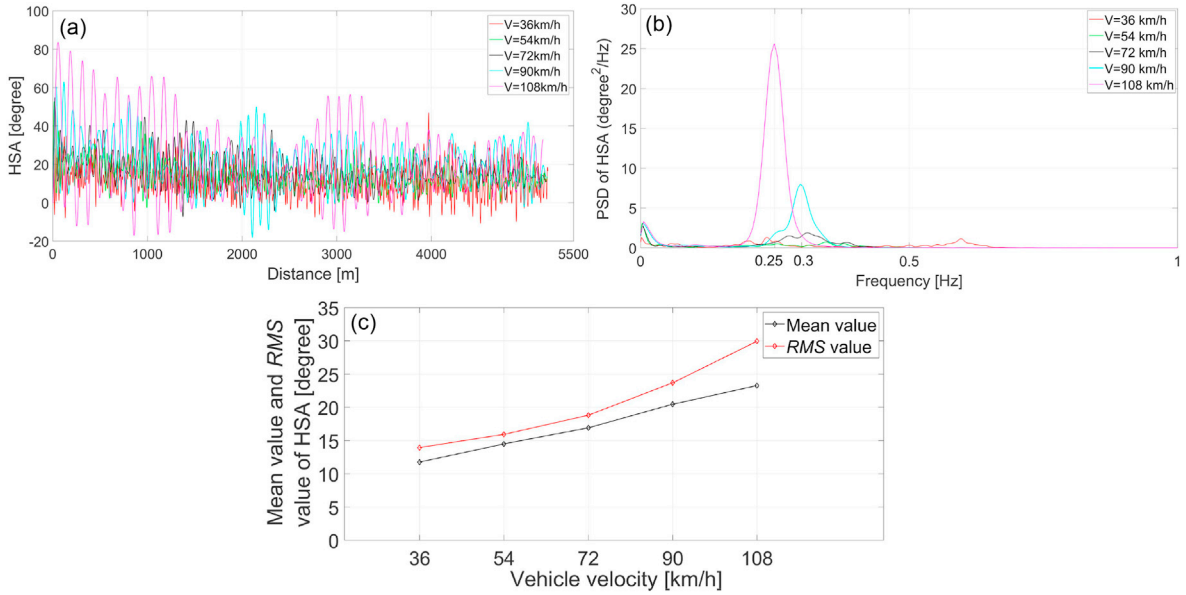

Fig. 22. HSA as a function of a) distance; b) frequency for different bus speeds; c) mean and RMS values of the HSA as a function of vehicle velocity.

5.1.2. *Driver steering effort*

Fig. 22a presents the HSA as a function of distance. The HSA intensities increase with increasing vehicle speed. Fig. 22b presents PSDs of the HSA. The intensities of the signals are below 0.5 Hz. The highest steering intensities are in the case of the 108 km/h bus speed, with the peak value at 0.25 Hz. At the speeds of 72 km/h and 90 km/h, the HAS intensities are concentrated around a frequency of 0.3 Hz. Under the influence of the cross-wind component, the HSA signals vary around some mean value. The mean value increases with increasing speed, which might cause some difficulty for the driver to control the vehicle. The *RMS* values of the HSA increase with increasing speed (Fig. 22c).

5.2. *Roll-over risk*

The total bus wheel load was calculated by Eqs. (30)-(33). Contact between the wheel and the road surface is lost when the total wheel load equals zero. Loosing contact between the bus wheel and bridge deck can indicate potential roll-over. (Reducing the vertical force also reduces the lateral grip, which is separately analysed in 5.3.)

Fig. 23 shows the total vertical force for each bus wheel as a function of time for speeds of 36 km/h, 90 km/h and 108 km/h. The vertical forces for the windward wheels are smaller than those for the leeward wheels. They have positive values for each speed except for the highest speed of 108 km/h. At the highest speed, variation in the vertical forces is noticeable soon after the bus enters the bridge. At approximately 2 s from the beginning of the simulation (at approximately 60 m of travelled distance), the windward rear wheel loses contact, indicating the potential risk of vehicle roll-over (Fig. 23c).

5.2.1. *Load transfer ratio (LTR)*

The *LTR* indicator is usually used to predict roll-over situations (Kamnik et al., 2003). It can be defined for each axle (Eq. (56)) or for the whole vehicle (Eq. (57)):

$$LTR_{fa} = \frac{Z_{tfl} - Z_{tfr}}{Z_{tfl} + Z_{tfr}}, \quad LTR_{ra} = \frac{Z_{trl} - Z_{trr}}{Z_{trl} + Z_{trr}} \tag{56}$$

$$LTR_{v} = \frac{Z_{tfl} + Z_{trl} - Z_{tfr} - Z_{trr}}{Z_{tfl} + Z_{tfr} + Z_{trl} + Z_{trr}} \tag{57}$$

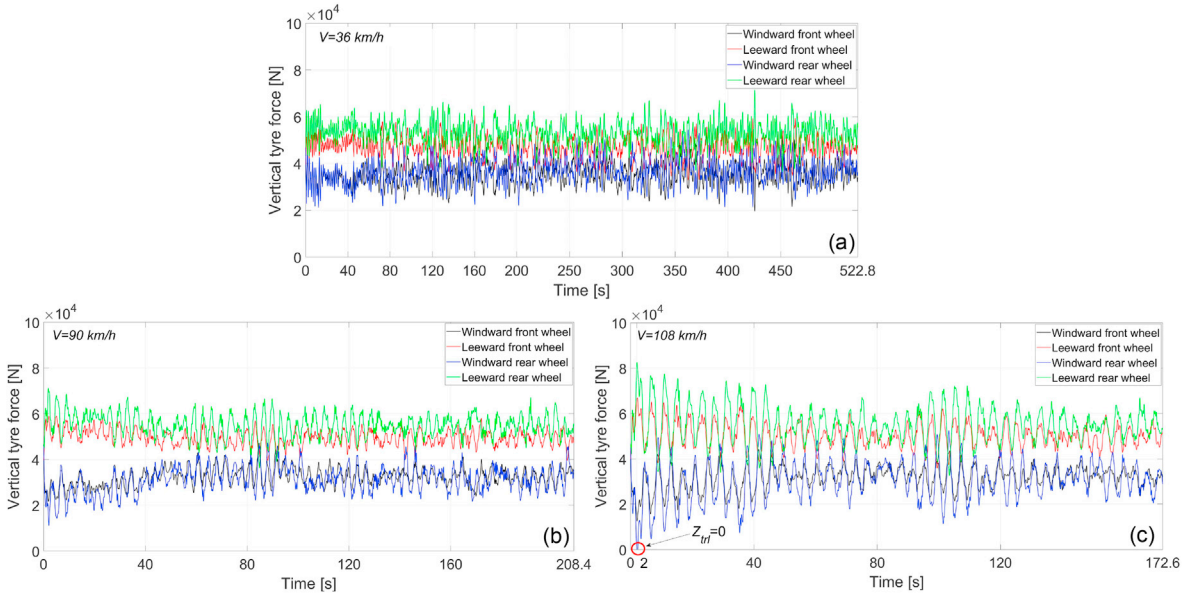

Fig. 23. Vertical tyre forces for bus speeds of a) 36 km/h; b) 90 km/h; c) 108 km/h.

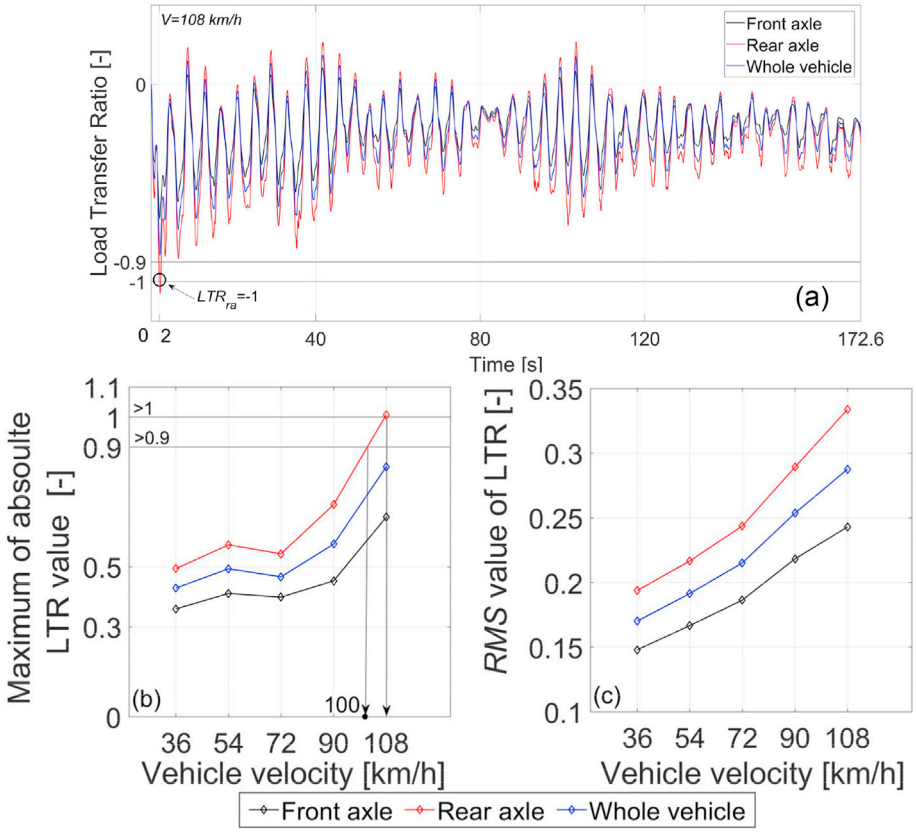

Fig. 24. a) LTR for bus speed of 108 km/h as a function of time; b) maximum absolute LTR value as a function of vehicle velocity; b) RMS value of LTR as a function of vehicle velocity.

The *LTR* parameter for an axle (front or rear, Eq. (56)) has often been used as a criterion for vehicle overturning (one tyre loses contact with the ground) (Cheli et al., 2006). If the absolute LTR_{fa} or LTR_{ra} value is larger than 0.9, the vehicle is considered to overturn. If the *LTR* for the whole vehicle is used (Eq. (59)), the left or right vehicle tyres lose contact with the ground if the absolute value is larger than 0.9, and the vehicle is considered to overturn (Wang, 2016).

Fig. 24a presents the *LTR* parameter for the front/rear axle and for the whole vehicle for a speed of 108 km/h. The windward rear wheel loses contact at one instance of time at approximately 2 s of simulation time.

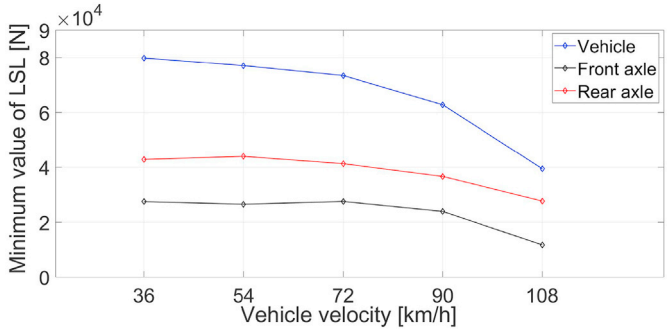

Fig. 25. Minimum LSL value as a function of vehicle velocity.

Fig. 24b shows the maximum absolute LTR value, and Fig. 24c shows the RMS values of the LTR parameter. The maximum absolute LTR value is an indicator of vehicle roll-over risk. For the rear axle, this value is larger than 0.9 for speeds above 100 km/h, indicating vehicle roll-over (Fig. 24b). The RMS values indicate vehicle roll-over risk due to wheel lift-off on the rear axle (Fig. 24c).

5.3. Risk of losing lateral grip

5.3.1. Lateral sideslip limit (LSL)

The LSL is based on the criterion that the minimum value of the difference between the maximum allowable lateral friction forces of all wheels and the actual lateral tyre forces should be equal to or greater than zero (Chen and Chen, 2011), Eq. (58)

$$\begin{aligned} LSL &= \min\left[F_{y,fa}^{max} + F_{y,ra}^{max} - \left(F_{y,fa} + F_{y,ra}\right)\right] \\ &= \min\left[\mu \cdot \left(Z_{t,fa} + Z_{t,ra}\right) - \left(F_{y,fa} + F_{y,ra}\right)\right] \geqslant 0 \end{aligned} \tag{58}$$

The LSL can also be defined for the front and rear bus axles, such as

$$\begin{aligned} LSL_{fa} &= min\left[F_{y,fa}^{max} - F_{y,fa}\right] = \min\left[\mu \cdot Z_{t,fa} - F_{y,fa}\right] \\ &= \min\left[\mu \cdot \left(Z_{tfl} + Z_{tfr}\right) - F_{y,fa}\right] \geqslant 0 \end{aligned} \tag{59}$$

$$\begin{aligned} LSL_{ra} &= \min\left[F_{y,ra}^{max} - F_{y,ra}\right] = \min\left[\mu \cdot Z_{t,ra} - F_{y,ra}\right] \\ &= \min\left[\mu \cdot \left(Z_{trl} + Z_{trr}\right) - F_{y,fa}\right] \geqslant 0 \end{aligned} \tag{60}$$

where $F_{y,fa}^{max}$ and $F_{y,ra}^{max}$ are respectively the maximum allowable lateral friction forces on the front and rear axle for the road surface; $Z_{z,fa}$ and $Z_{z,ra}$ are respectively the vertical forces on the front and rear bus axle defined by Eqs. (30)-(33); $F_{y,fa}$ and $F_{y,ra}$ are respectively the actual lateral tyre forces for the front and rear bus axle defined by Eq. (29); and μ is the road friction coefficient for dry/wet asphalt (value of 0.7). If the LSL is less than zero for the whole vehicle, the front or rear axle starts to sideslip.

Fig. 25 shows the minimum LSL value for the whole vehicle and for the front and rear bus axles as a function of speed. The LSL is greater than zero for each case, meaning that for the considered road surface, the LSL limit is not reached.

6. Conclusion

In this research, bus behaviour when passing across a floating bridge under environmental loads (1-year storm condition case) was analysed. For this purpose, 8 DOF bus model and pure pursuit driver model were defined. The bus model was excited with bridge motion signals and wind components.

From this research, the main conclusions are as follows:

- The vehicle deviation from the path increases with increasing bus speed. Deviation from the path is significant after the vehicle enters the bridge at a high speed when a high-velocity cross-wind load starts acting (e.g., for a speed of 90 km/h, the deviation is over 0.5 m; for a speed of 108 km/h, the deviation is very large, up to 2 m).
- The path deviation changes along the length of the bridge depending on the bus speed, wind and bridge motion excitations. The largest path deviations are for the case of 108 km/h soon after the bus enters the bridge and remain at a high value (approximately 0.5 m) along the bridge. At a travelled distance of approximately 2 km from entering the bridge, the lateral displacements are close to 0.5 m for a velocity of 90 km/h.
- Under wind loads from 1-year storm conditions, simulation results suggest that a bus might start driving at a lower speed (e.g., 72 km/h) with the possibility of increasing the speed (up to 90 km/h) at the lower part of the bridge (after approximately 2 km). This conclusion is similar to recommendations based on driving simulator tests for buses running in straight lines across bridges. The recommendation suggests *"straight line driving for the bus at* 90 km/h *up to weather 6 (1-year storm condition)"*.
- Under the influence of the cross-wind component, the HSA signals oscillate around a mean value. The mean HSA value increases with increasing speed, which might cause some difficulty for the driver to control the vehicle. The HSA intensities increase with increasing bus speed. The intensities of the signals are below 0.5 Hz. The highest steering intensities are in the case of 108 km/h, with slightly lower frequencies in comparison to the signals for bus speeds of 72 km/h and 90 km/h.
- Vertical forces for the windward wheels have lower values than those for the leeward wheels. At the highest speed, variation in the vertical forces is noticeable when the bus enters the bridge. At 2 s from the beginning of the simulation (at a travelled distance of approximately 60 m from entering the bridge), the windward rear wheel loses contact, indicating the potential risk of vehicle roll-over. This is also confirmed with LTR parameters.
- The LSL values are greater than zero, meaning that there is no sideslip for the front/rear axle or whole vehicle for the considered road surface (wet/dry condition with a peak road friction coefficient of 0.7).

CRediT authorship contribution statement

Dragan Sekulic: Conceptualization, Methodology, Data curation, Visualization, Writing – original draft, Writing – review & editing. **Alexey Vdovin:** Supervision, Conceptualization, Writing – review & editing. **Bengt Jacobson:** Supervision, Conceptualization, Methodology, Validation. **Simone Sebben:** Supervision, Conceptualization, Writing – review & editing. **Stian Moe Johannesen:** Investigation, Resources, Writing – review & editing.

Declaration of competing interest

The authors declare that they have no known competing financial interests or personal relationships that could have appeared to influence the work reported in this paper.

Acknowledgements

Support for this research was provided by The Norwegian Public Roads Administration (NPRA). This support is gratefully acknowledged. The aerodynamic simulations were performed on resources provided by the Swedish National Infrastructure for Computing (SNIC).

7 Appendix

Table 1
Intercity bus parameters

Geometric parameters of the bus	
Wheelbase L [m]	8.375
Distance from front axle to centre of gravity (CoG) of an empty bus l_f [m]	4.4103
Distance from rear axle to CoG of an empty bus l_r [m]	3.9647
Distance from the front right/left wheel to the front axle CoG b_f [m]	1.00
Distance from the rear right/left wheel to the rear axle CoG b_r [m]	1.00
Distance from the CoG of the whole vehicle to the ground $h_{CoG,\ stat.}$ [m]	1.1725
Height of the front axle roll-centre $h_{RCfa,\ stat.}$ [m]	0.508
Height of the rear axle roll-centre $h_{RCra,\ stat.}$ [m]	0.508
Distance from the CoG to the roll-centre for the front axle $h_{RCfa,\ stat.}$ [m]	0.6645
Distance from the CoG to the roll-centre for the rear axle $h_{RCra,\ stat.}$ [m]	0.6645
Distance from suspension elements on the front axle to the front axle CoG e_{u1} [m]	0.70
Distance from suspension elements on the rear axle to the rear axle CoG e_{u2} [m]	0.80
Mass parameters of the bus	
Sprung mass of the empty bus m_s [kg]	16099
Front axle mass m_{u1} [kg]	746
Rear axle mass m_{u2} [kg]	1355
Mass of the empty bus m [kg]	18200
Sprung mass moment of inertia about its x-axis J_{sx} [kgm^2]	33400
Moment of inertia of the bus about z-axis J_z [kgm^2]	290000
Front axle moment of inertia relative to the x_1-axis J_{u1x1} [kgm^2]	315
Rear axle moment of inertia relative to the x_2-axis J_{u2x2} [kgm^2]	657
Oscillatory parameters of the bus	
Single air spring stiffness on the front axle k_{sf} [N/m]	175000
Equivalent air spring stiffness on the front axle k_{sfeq} [N/m]	350000
Single shock-absorber damping on the front axle c_{df} [Ns/m]	20000
Equivalent shock-absorber damping on the left side of the front axle c_{dfl} [Ns/m]	40000
Equivalent shock-absorber damping on the right side of the front axle c_{dfr} [Ns/m]	40000
Equivalent shock-absorber damping on the front axle c_{dfeq} [Ns/m]	80000
Single air spring stiffness on the rear axle k_{sr} [N/m]	200000
Equivalent air spring stiffness on the left side of the rear axle k_{srl} [N/m]	400000
Equivalent air spring stiffness on the right side of the rear axle k_{srr} [N/m]	400000
Equivalent air spring stiffness on the rear axle k_{sreq} [N/m]	800000
Single shock-absorber damping on the rear axle c_{dr} [Ns/m]	22500
Equivalent shock-absorber damping on the left side of the rear axle c_{drl} [Ns/m]	45000
Equivalent shock-absorber damping on the right side of the rear axle c_{drr} [Ns/m]	45000
Equivalent shock-absorber damping on the rear axle c_{dreq} [Ns/m]	90000
Tyre radial stiffness on the left/right side on front axle k_{tfl}/k_{tfr} [N/m]	1000000
Equivalent radial tyre stiffness on the front axle k_{tfeq} [N/m]	2000000
Tyre radial stiffness on the left/right side on rear axle k_{trl}/k_{trr} [N/m]	2000000
Equivalent radial tyre stiffness on the rear axle k_{treq} [N/m]	4000000
Anti-roll bar torsional stiffness on front axle K_{arbf} [Nm/rad]	120000
Anti-roll bar torsional stiffness on rear axle K_{arbr} [Nm/rad]	120000
Roll stiffness for the front axle $K_{\phi f}$ [Nm/rad]	171500
Roll damping for front axle $C_{\phi f}$ [Nms/rad]	39200
Roll stiffness for the rear axle $K_{\phi r}$ [Nm/rad]	512000
Roll damping for rear axle $C_{\phi r}$ [Nms/rad]	57600

Table 2
Other notations

O_1xyz	Vehicle coordinate system
Δ	Steering angle for front vehicle left/right wheel [rad]
ϕ_{xs}, ϕ_{x1}, ϕ_{x2}	Roll-angle motion for the vehicle body, front axle, rear axle [rad]
ω_{xs}, ω_{x1}, ω_{x2}	Roll-angle rate for the vehicle body, front axle, rear axle [rad/s]
$\dot{\omega}_{xs}$, $\dot{\omega}_{x1}$, $\dot{\omega}_{x2}$	Roll-angle acceleration for the vehicle body, front axle, rear axle [rad/s^2]
z, $\dot{z}$, $\ddot{z}$	Vertical motion/velocity/acceleration of the vehicle body [m; m/s; m/s^2]
z_1, $\dot{z}_1$, $\ddot{z}_1$	Vertical motion/velocity/acceleration of the bus front axle [m; m/s; m/s^2]
z_2, $\dot{z}_2$, $\ddot{z}_2$	Vertical motion/velocity/acceleration of the bus rear axle [m; m/s; m/s^2]
$\dot{v}_y$	Lateral acceleration of the bus CoG in vehicle fixed coordinate system [m/s^2]
a_y	Total lateral acceleration of the bus CoG in vehicle fixed coordinate system [m/s^2]
v_x, v_y	Longitudinal/lateral velocity of the bus CoG in vehicle fixed coordinate system [m/s]
Ψ, ω_z, $\dot{\omega}_z$	Vehicle yaw motion/rate/acceleration [rad; rad/s; rad/s^2]
s_{fy}, s_{ry}	Lateral tyre slip for the wheels on the front/rear axle [-]
ζ_{tfr}, ζ_{tfl}	Vertical excitations on the front right/left wheel
ζ_{trr}, ζ_{trl}	Vertical excitations on the rear right/left wheel
ζ_{fa}, ζ_{ra}	Road roughness below front/rear axle CoGs
ζ_1	Road roughness below rotational centre of sprung mass (RC)
μ	Road friction coefficient (dry/wet asphalt) 0.7 [-]
$v_{y\ br,fa}$, $v_{y\ br,ra}$	Lateral velocity of the bridge deck at the tyre contact point for the front/rear bus axle [m/s]
C_{cy}	Cornering stiffness coefficient 7 [(N/rad)/N]

(*continued on next column*)

Table 2 (*continued*)

O_1xyz	Vehicle coordinate system
Δh_{sm}	Vertical distance from CoG to vehicle roll-axis (point *RC*)
Δh_{sf}, Δh_{sr}	Vertical distance from CoG of the bus sprung mass to front/rear axle roll centres
ρ	Air density 1.29 [kg/m^3]

References

Bhat, A.B., et al., 2020. *Driver Influence on Vehicle Track-Ability on Floating Bridges*. TME180 Automotive Engineering Project. Chalmers University of Technology, Gothenburg, Sweden. https://odr.chalmers.se/handle/20.500.12380/300748.

Branlard, E., 2010. Wind Energy: Generation of Time Series from a Spectrum. Technical University of Denmark, Denmark.

Cheli, F., Belforte, P., Melzi, S., Sabbioni, E., Tomasini, G., 2006. Numerical–experimental approach for evaluating cross-wind aerodynamic effects on heavy vehicles. Veh. Syst. Dyn. 44 (Suppl. 1), 791–804.

Chen, F., Chen, S., 2011. Reliability-based assessment of vehicle safety in adverse driving conditions. Transport. Res. C Emerg. Technol. 19 (1), 156–168.

Chen, S.R., Cai, C.S., 2004. Accident assessment of vehicles on long-span bridges in windy environments. J. Wind Eng. Ind. Aerod. 92 (12), 991–1024.

Drugge, L., Juhlin, M., 2010. Aerodynamic loads on buses due to crosswind gusts: extended analysis. Veh. Syst. Dyn. 48 (S1), 287–297.

Gillespie, T., 1992. Fundamentals of Vehicle Dynamics. SAE, Warrendale PA, USA.

Gustafsson, A., et al., 2019. Driver Influence on Vehicle Track-Ability on Floating Bridges. Bachelor's Thesis in Mechanical Engineering. Department of Mechanics and Maritime Sciences, Chalmers University of Technology, Gothenburg, Sweden. https://odr.chalmers.se/handle/20.500.12380/256914.

Hellsten, O., et al., 2020. Aerodynamic Investigations of a Bus under High Side Wind Conditions. TME180 Automotive Engineering Project. Chalmers University of Technology, Gothenburg, Sweden. https://odr.chalmers.se/handle/20.500.12380/301635.

ISO, 8608, 1995. Mechanical Vibration-Road Surface Profiles-Reporting of Measured Data. International Standards Organization, Switzerland.

Jacobson. Vehicle Dynamics Compendium. Chalmers University of Technology. https://research.chalmers.se/publication/513850/file/513850_Fulltext.pdf.

Juhlin, M., 2009. Assessment of Crosswind Performance of Buses. PhD Thesis. KTH. https://www.diva-portal.org/smash/get/diva2:216431/FULLTEXT01.pdf.

Kamnik, R., Boettiger, F., Hunt, K., 2003. Roll dynamics and lateral load transfer estimation in articulated heavy freight vehicles. Automobile Eng. Proc. Inst. Mech. Eng, Part D: J. Automobile Eng. 217 (11), 985–997.

Liu, P.J., Rakheja, S., Ahmed, A.K.W., 2001. Dynamic roll instability analysis of heavy vehicles using energy approach. Int. J. Heavy Veh. Syst. 8 (2), 177–195.

Nguyen, V.M., Le, V.Q., 2019. Ride comfort performance of heavy truck with three control cases of semi-active isolation systems. Vibroeng. Procedia 22, 93–98.

Salati, L., Schito, P., Rocchi, D., Sabbioni, E., 2018. Aerodynamic study on a heavy truck passing by a bridge pylon under crosswinds using CFD. J. Bridge Eng. 23 (9), 04018065.

Schuetz, T.C., 2015. Aerodynamics of Road Vehicles, Fifth Edition. SAE International.

Sekulic, D., 2018. Effect of Floating Bridge Vertical Motion on Vehicle Ride Comfort and Road Grip. https://www.vegvesen.no/_attachment/2487039/binary/1294853?fast_title=Effect+of+floating+bridge+vertical+motion+on+vehicle+ride+comfort+and+road+grip.pdf.

Sekulic, D., et al., 2013. Analysis of vibration effects on the comfort of intercity bus users by oscillatory model with ten degrees of freedom. Appl. Math. Model. 37 (18), 8629–8644.

Sekulic, D., Jacobson, B., Moe, S.J., Svangstu, E., 2020. Effect of floating bridge motion on vehicle ride comfort and road grip. In: The IAVSD International Symposium on Dynamics of Vehicles on Roads and Tracks. Springer, Cham, pp. 1416–1424.

Shinozuka, M., 1972. Digital simulation of random processes and its applications. J. Sound Vib. 25 (1), 111–128.

Siringoringo, D.M., Fujino, Y., 2012. Estimating bridge fundamental frequency from vibration response of instrumented passing vehicle: analytical and experimental study. Adv. Struct. Eng. 15 (3), 417–434.

Snider, M.J., 2009. Automatic Steering Methods for Autonomous Automobile Path Tracking. CMU-RI-TR-09-08.

Vegvesen, 2017. SBJ-31-C3-MUL-22-RE-100 - Analysis and Design (Base Case) Bjørnafjorden, Straight Floating Bridge Phase 3 Analysis and Design (Base Case).

Wang, B., Xu, Y., Li, Y., 2016. Nonlinear safety analysis of a running road vehicle under a sudden crosswind. J. Transport. Eng. 142 (2), 04015043.

William, Y., et al., 2014. Analysis of vehicle lateral dynamics due to variable wind gusts. SAE Int. J. Commer. Veh. 7 (2), 666–674.

Yu, N., 2007. Yaw-control Enhancement for Buses by Active Front-Wheel Steering. PhD Thesis. The Pennsylvania State University. https://www.mne.psu.edu/toboldlygo/Publications/Theses/2007_Yu_PhD.pdf.

Zhang, Q., Su, C., Zhou, Y., Zhang, C., Ding, J., Wang, Y., 2020. Numerical investigation on handling stability of a heavy tractor semi-trailer under crosswind. Appl. Sci. 10 (11), 3672.

Zhou, Y., Chen, S., 2015. Fully coupled driving safety analysis of moving traffic on long-span bridges subjected to crosswind. J. Wind Eng. Ind. Aerod. 143, 1–18.